

Evidence for the contemporary magmatic system beneath Long Valley Caldera from local earthquake tomography and receiver function analysis

D. Seccia,^{1,2} C. Chiarabba,¹ P. De Gori,¹ I. Bianchi,^{1,3} and D. P. Hill⁴

Received 21 April 2011; revised 5 October 2011; accepted 12 October 2011; published 23 December 2011.

[1] We present a new P wave and S wave velocity model for the upper crust beneath Long Valley Caldera obtained using local earthquake tomography and receiver function analysis. We computed the tomographic model using both a graded inversion scheme and a traditional approach. We complement the tomographic V_p model with a teleseismic receiver function model based on data from broadband seismic stations (MLAC and MKV) located on the SE and SW margins of the resurgent dome inside the caldera. The inversions resolve (1) a shallow, high-velocity P wave anomaly associated with the structural uplift of a resurgent dome; (2) an elongated, WNW striking low-velocity anomaly (8%–10 % reduction in V_p) at a depth of 6 km (4 km below mean sea level) beneath the southern section of the resurgent dome; and (3) a broad, low-velocity volume (~5% reduction in V_p and as much as 40% reduction in V_s) in the depth interval 8–14 km (6–12 km below mean sea level) beneath the central section of the caldera. The two low-velocity volumes partially overlap the geodetically inferred inflation sources that drove uplift of the resurgent dome associated with caldera unrest between 1980 and 2000, and they likely reflect the ascent path for magma or magmatic fluids into the upper crust beneath the caldera.

Citation: Seccia, D., C. Chiarabba, P. De Gori, I. Bianchi, and D. P. Hill (2011), Evidence for the contemporary magmatic system beneath Long Valley Caldera from local earthquake tomography and receiver function analysis, *J. Geophys. Res.*, 116, B12314, doi:10.1029/2011JB008471.

1. Introduction

[2] Long Valley Caldera is a late Tertiary-Quaternary volcanic system located in central California (Figure 1), within a left stepping offset along the eastern escarpment of the Sierra Nevada at the western margin of the Basin and Range Province [Hill, 2006]. The caldera was formed 0.76 Ma ago during the massive eruption of the Bishop Tuff (600 km³ solid rock equivalent), coincident with 1–2 km of subsidence of an elliptical block (17 × 32 km) into the partially evacuated magma chamber. After the caldera formation, smaller rhyolitic eruptions centered on the resurgent dome were fed by the residual magma chamber culminating in eruptions around the margin of the resurgent dome at 500 ka, 300 ka and 100 ka ago [Bailey, 1976; Hildreth, 2004]. Most recently (110–40 ka), volcanic activity shifted to the west, with repeated eruptions between 110 and 50 ka forming Mammoth Mountain on the southwest margin of the caldera and a series of eruptions from 40 ka to ~300 ybp forming the

Mono-Inyo volcanic chain, which extends 50 km to the north [Hildreth, 2004].

[3] Beginning in late 1978, Long Valley Caldera experienced intense unrest with earthquake swarms, uplift of the resurgent dome, and CO₂ emission around Mammoth Mountain [Langbein *et al.*, 1993; Hill and Prejean, 2005; Prejean *et al.*, 2003; Hill, 2006]. The intracaldera deformation has been modeled by a volumetric source located at 5–8 km depth beneath the dome, along with slip on faults in the south moat [Langbein, 2003]. The density of the deformation source is consistent with a magmatic or hybrid source (magma + fluids) [Battaglia *et al.*, 1999, 2003b]. A recent study based on InSAR and gravity measurements [Tizzani *et al.*, 2009] found evidence that the uplift is a result of a magmatic intrusion of ~0.07 km³ of beneath the resurgent dome between 1992 and 1999.

[4] Despite evidence from geodetic and seismicity data [e.g., Langbein, 2003; Battaglia *et al.* 1999, 2003a, 2003b; Tizzani *et al.*, 2009; Prejean *et al.*, 2002] in support of a magmatic source in the shallow crust, seismic tomography studies have yet to find clear, well-resolved P wave or S wave velocity anomalies supporting such a structure. Previous studies indicate that seismic data are consistent with magma at shallow depths (<7 km below the surface) [see Hill, 1976; Sanders *et al.*, 1995; Steck and Prothero, 1994], but the location and geometry of the magma body are poorly

¹INGV, CNT, Rome, Italy.

²Dipartimento di Fisica, Università di Bologna, Bologna, Italy.

³Institut für Meteorologie und Geophysik, Universität Wien, Vienna, Austria.

⁴U.S. Geological Survey, Menlo Park, California, USA.

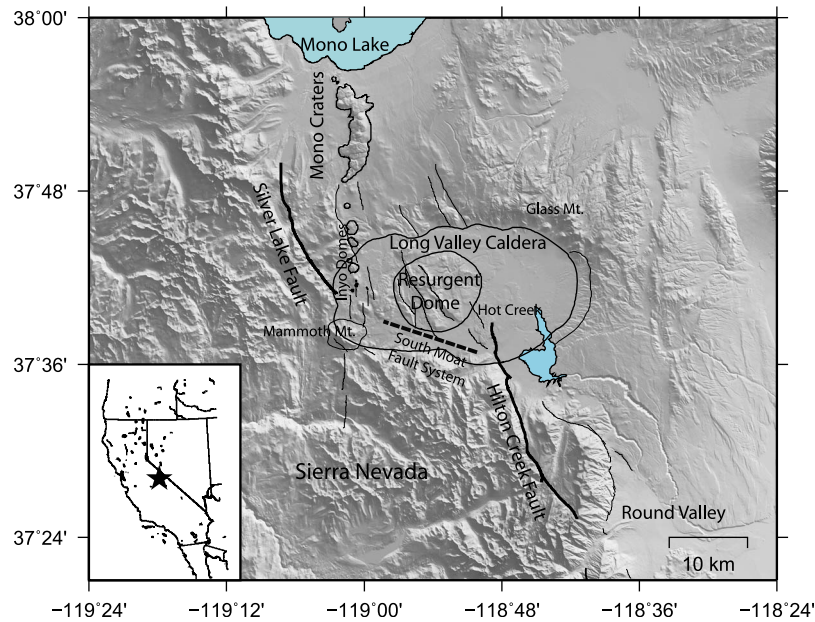


Figure 1. Shaded relief map of the Long Valley Caldera area. Thin black lines designate the caldera and resurgent dome boundaries and the major faults in the Long Valley area. Thick black lines are the Sierra Nevada range bounding normal faults. Star in the inset map of the western United States shows the location of the Long Valley area.

constrained. *Kissling* [1988] noted the absence of a large midcrustal magma chamber beneath the caldera. Lithological variations, state of fluid phases and temperature are the main factors influencing wave speed heterogeneity beneath active volcanoes [*O'Connell and Budiansky*, 1977; *Mavko*, 1980; *Sato et al.*, 1989]. Low V_p characterize magma chambers and zones of partial melt, while high- V_p velocities are consistent with dense intrusive bodies [*Iyer et al.*, 1990; *Chiarabba et al.*, 2000]. Broad low- V_p or low- Q_p (high P wave attenuation) volumes are revealed by teleseismic tomography in the middle crust [*Dawson et al.*, 1990; *Weiland et al.*, 1995] and at 8 km depth beneath the entire caldera [*Romero et al.*, 1993; *Ponko and Sanders*, 1994], which were interpreted as a zone of partial melt. *Foulger et al.* [2003] find evidence for temporal variation of V_p and V_p/V_s anomalies indicating a progressive depletion of CO_2 fluids at shallow depth beneath Mammoth Mountain, but do not resolve anomalies deeper than 3–4 km depth.

[5] The aim of this study is to provide new information on the magma plumbing system of the caldera by combining two techniques, local earthquake tomography (LET) and teleseismic receiver functions (RFs) to improve resolution of both shallow and deeper crustal structures. LET has been widely employed to investigate volcanoes [*Ellsworth and Koyanagi*, 1977; *Thurber*, 1984; *Evans and Zucca*, 1993; *Lees*, 1992; *Benz et al.*, 1996; *Mori et al.*, 1996; *Chiarabba et al.*, 2000; *Di Stefano and Chiarabba*, 2002; *Chiarabba and Moretti*, 2006; *De Gori et al.*, 2005]. The RFs technique is an innovative but still not thoroughly explored method to investigate volcanoes [*Chmielowski et al.* 1999; *Darbyshire et al.* 2000; *Nakamichi et al.* 2002].

[6] *Piana Agostinetti and Chiarabba* [2008] initially used LET and RFs together to investigate the Mount Vesuvio plumbing system. The joint interpretations of results by these

two techniques helped identify a localized melt volume enclosed between two solidified bodies in the volcano axis.

[7] We developed tomographic inversions using local earthquake sources through both direct and graded schemes, in which subsequent inversions are carried out focusing gradually on the best sampled crustal volume. We then used RFs from teleseismic data recorded at two permanent broadband stations (MLAC and MKV) installed inside the caldera around the resurgent dome to constrain the S wave velocity structure in the crust. RFs were analyzed and inverted using the Neighborhood Algorithm approach. We jointly interpret the one-dimensional shear wave velocity (1-D V_s) profile with the P wave velocity (V_p) model obtained by tomographic inversion and discuss the significance of the result.

[8] We take mean sea level (msl) as the reference elevation. Note that the mean surface (or station) elevation (mse) within the caldera is ~ 2.3 km above sea level.

2. Methodology

2.1. Local Earthquake Tomography

[9] The inversions are performed following the method developed by *Thurber* [1983] and *Um and Thurber* [1987], as modified by *Eberhart-Phillips* [1993] and *Eberhart-Phillips and Reyners* [1997]. The technique uses P wave arrival times to invert simultaneously for hypocentral and velocity parameters. The velocity is continuously defined within the volume by using a linear interpolation among the adjacent nodes. The solution is obtained by using an iterative damped least squares algorithm. The damping value is chosen to optimize the data misfit and model complexity. The procedure is iterated until the variance improvement ceases to be significant, according to an F test.

Table 1. Inversion Parameters

Model	Grad-1	Grad-2	Grad-3
Area (km)	48 × 48	36 × 36	18 × 18
Horizontal grid spacing (km)	6	4	2
Number of layers	9	8	7
Depth of layers (km)	-2, 0, 2, 4, 6, 9, 12, 15, 18	-2, 0, 2, 4, 6, 9, 12, 15	-2, 0, 2, 4, 6, 8, 10
Number of earthquakes used	1814	1517	471
Number of <i>P</i> phases	40727	29412	7503
Number of stations	46	35	24
Inverted parameters	933	965	813
Iteration steps	4	4	4
Damping factor	1000	400	60
Final RMS (s)	0.04689	0.04363	0.04639

[10] Considering the seismic network geometry and the uneven distribution of seismicity in the Long Valley area, we develop a progressively more detailed image of the structure beneath the caldera using a graded inversion scheme [Chiarabba *et al.*, 1995; Eberhart-Phillips 1990, 1993]. The velocity model is parameterized assigning velocity values of the previously used 1-D velocity model to a 3-D grid of nodes. Subsequent inversions are carried out decreasing the grid spacing from a coarse to a fine grid in the best sampled crustal volume. The model calculated at each step is used as the input model for the subsequent inversion.

[11] To test the reliability of the tomographic models, we perform an analysis of the Resolution Matrix (RM). Each row of RM contains information on the volumetric estimate of parameters. A perfectly resolved node is characterized by a compact averaging vector with elements close to 1 on the diagonal and 0 elsewhere. The sharpness of the averaging vector is quantified by means of the Spread Function (SF) as defined by *Michellini and McEvilly* [1991]. The SF compresses each row of the resolution matrix into a single number that describes how strong and peaked the resolution is for that node [Toomey and Foulger, 1989]. The smaller the SF value, the better the resolution for the model parameter.

2.2. Receiver Function

[12] We computed RFs by deconvolution of the vertical from the radial (R) and transverse (T) horizontal components [see *Langston*, 1979]. RFs are calculated through a frequency domain deconvolution [Di Bona, 1998] using a Gaussian filter ($a = 2$) to limit the final frequency band below about 1 Hz. A better signal-to-noise ratio is achieved by stacking the RFs coming from the same back azimuth direction (Φ) and epicentral distance (Δ) [Park *et al.*, 2004]. RFs are stacked in 50% overlapping bins of back azimuth (BAZ) 20°, and epicentral distance 40°.

[13] To model data, we apply a forward modeling procedure using the Neighborhood Algorithm (NA) to iteratively sample the good data-fitting region of an initial parameter space (for details [see *Sambridge*, 1999a, 1999b].) Following the original implementation of the NA, we initially generated 1000 samples evenly distributed in the parameter space. From the best fit models, 20 new samples were iteratively resampled. After 1000 iterations, we obtained an ensemble of 21,000 models. We computed synthetic seismograms using the RAYSUM code, which models the propagation of

a plane wave in dipping and/or anisotropic structure [Frederiksen and Bostock, 2000].

3. Data Analysis and Results

3.1. Seismic Data and Tomographic Modeling

[14] Seismic data used for LET are those recorded by the Northern California Seismic Network (NCSN) during the period 2002–2008. Seismicity is concentrated in the Sierra block south of the caldera and in the south moat fault zone. Most of the seismicity occurred at depths between 5 and 15 km (below msl) with a cluster of deeper earthquakes centered at ~25 km directly beneath Mammoth Mountain, most of them occurring during June 2006 (models grad-1, grad-2, and grad-3 with horizontal node spacing decreasing from 6 km to 4 km to 2 km, respectively, see Table 1).

[15] We first locate a total of 7090 local earthquakes with the Hypoellipse code [Lahr, 1989] and a one-dimensional (1-D) starting model derived from previous tomographic studies [Kissling, 1988; Steck and Prothero, 1994; Weiland *et al.*, 1995]. We then select a subset of 1814 earthquakes with at least 14 *P* wave arrivals, azimuthal gap less than 140°, and location uncertainty less than 2 km, with most having a location uncertainty less than 1 km (Figure 2).

[16] A total of 40,727, 29,412 and 7503 *P* wave arrivals are inverted in the three progressive steps of the graded inversion using damped least squares.

[17] For each step of the 3-D inversion, the damping factor was selected by performing a trade-off analysis of the data and the model variances. The resulting value was then used in the damped least squares inversion. Values of damping factor in the three graded steps and other statistical parameters are reported in Table 1.

[18] For depths greater than 4 km below msl we rely primarily on the grad-2 model (Figures 3 and 4), which shows a higher resolution than the grad-3 model. Between the surface (-2 km) and 2 km below msl, the grad-2 and grad-3 model results (Figures 3 and 5, respectively) reveal a high-velocity body centered beneath the resurgent dome (V_p ranging between 3.8 km/s and 4.6 km/s, anomaly C) bounded by an annular zone of low V_p (2.6–3.6 km/s) related to postcaldera fill. At 4 km below msl, a WNW trending, negative V_p anomaly (4.8–5.4 km/s) with map dimensions of ~5 by 10 km is present beneath the southern section of the resurgent dome (anomaly A). A similar anomaly (B) is located to the east of the dome, beneath the Hot Creek Flow. Both A and B anomalies are clearly visible in grad-2 and grad-3 models. At 6 km below msl, positive V_p anomalies ($V_p = 6.2$ km/s) are present beneath the western, southern and eastern portion of caldera rim; the southern high- V_p anomaly is coincident with the location of most of the seismicity. The deep, high- V_p anomalies surround a volume of reduced *P* wave velocity (anomaly E, 5.8 km/s) present beneath the entire caldera clearly visible in grad-2 and grad-3 models. The continuity of the positive velocity anomaly is interrupted beneath Mammoth Mountain by a localized low- V_p anomaly (Figures 3 and 5), anomaly D, $V_p = 5.6$ –5.8 km/s).

[19] Vertical sections of grad-3 model show the details of caldera structure (Figure 6). The high- V_p anomaly centered on the resurgent dome is clearly visible in all the sections down to 3 km below msl, sharply bounded by low V_p of the postcaldera fill. Beneath the shallow, high-velocity plug, we

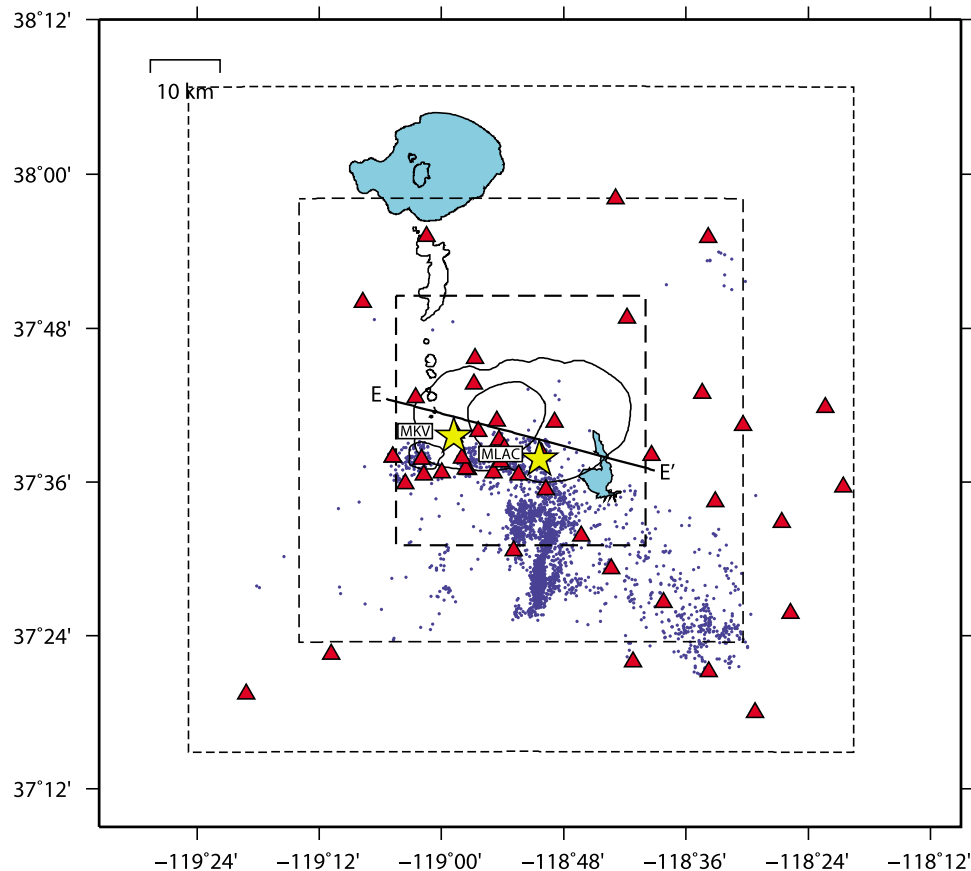


Figure 2. Map of the seismic stations (triangles) and earthquakes (blue dots) used in this study. Solid lines indicate the boundaries of the caldera and resurgent dome. The boxes outlined with black dashed lines indicate volumes covered by grad-1 (thin dashed line), grad-2 (medium dashed line), and grad-3 (thick dashed line) grids used in the graded inversion. Yellow stars show locations of broadband stations MKV and MLAC used in the receiver function analysis.

clearly resolve an elongated volume of lower P wave velocities. The deep, high- V_p anomaly, between 6 km and 10 km below msl, coincides closely with the caldera rim.

[20] We have relocated the seismicity that occurred between 1988 and 2008, using the computed 3-D velocity model. Average hypocentral shifts and uncertainties with respect to NCSN locations are on the order of 0.6 km and 0.03 s. The distribution of relocated seismicity reveals that the hypocenters are mostly concentrated on strike-slip and normal faults of the Sierra block and in the South Mouth area, as already revealed by previous studies [Prejean *et al.*, 2003]. We find no outstanding differences for earthquakes located within the caldera respect to locations obtained with the double difference technique [Waldhauser and Schaff, 2008] reinforcing the reliability of our 3-D velocity model.

[21] We also calculated a tomographic model using a direct inversion (nograd-3), with the same node spacing as grad-3 and using a 1-D model as the starting velocity model. We then compared these two models to show the differences in using the graded scheme with respect to the traditional approach to tomographic studies in Long Valley area (Figure 7). Compared with the direct approach, we noted that the graded-inversion scheme reproduces higher-amplitude anomalies. This is direct consequence of the higher resolution obtained by the graded inversion. The grad-3

model is more sensitive both to shallow and deep anomalies. We think the graded inversion scheme is more suitable than direct inversion for Long Valley area. The uneven distribution of seismicity and the inhomogeneous seismic station coverage around and inside the caldera preclude direct inversion from reliably resolving structural details inside the caldera. We take considerable care in applying the graded inversion scheme by jointly analyzing grad-2 and grad-3 models with an eye to known geologic constraints. In this way we minimize problems related to artifacts and smearing of anomalies in low-resolution regions into the finer, high-resolution model (grad-3).

[22] The reliability of the V_p models has been verified by using both a complete analysis of the resolution matrix (RM) and synthetic tests. In our case parameters with compact averaging vectors [see Toomey and Foulger, 1989; De Gori *et al.*, 2005] have SF values smaller than 3. From the analysis of the derivative weight sum (DWS) [Toomey and Foulger, 1989] versus spread function (Figure 8) for grad-2 and grad-3 models we choose 3 as cutoff value of SF for both grad-2 and grad-3 models. Because the SF is computed by summing the contribution of all nodes, it gives no information on the directional properties of the parameter estimation (smearing). To analyze the smearing directions we contoured, for each node, the volume where the resolution

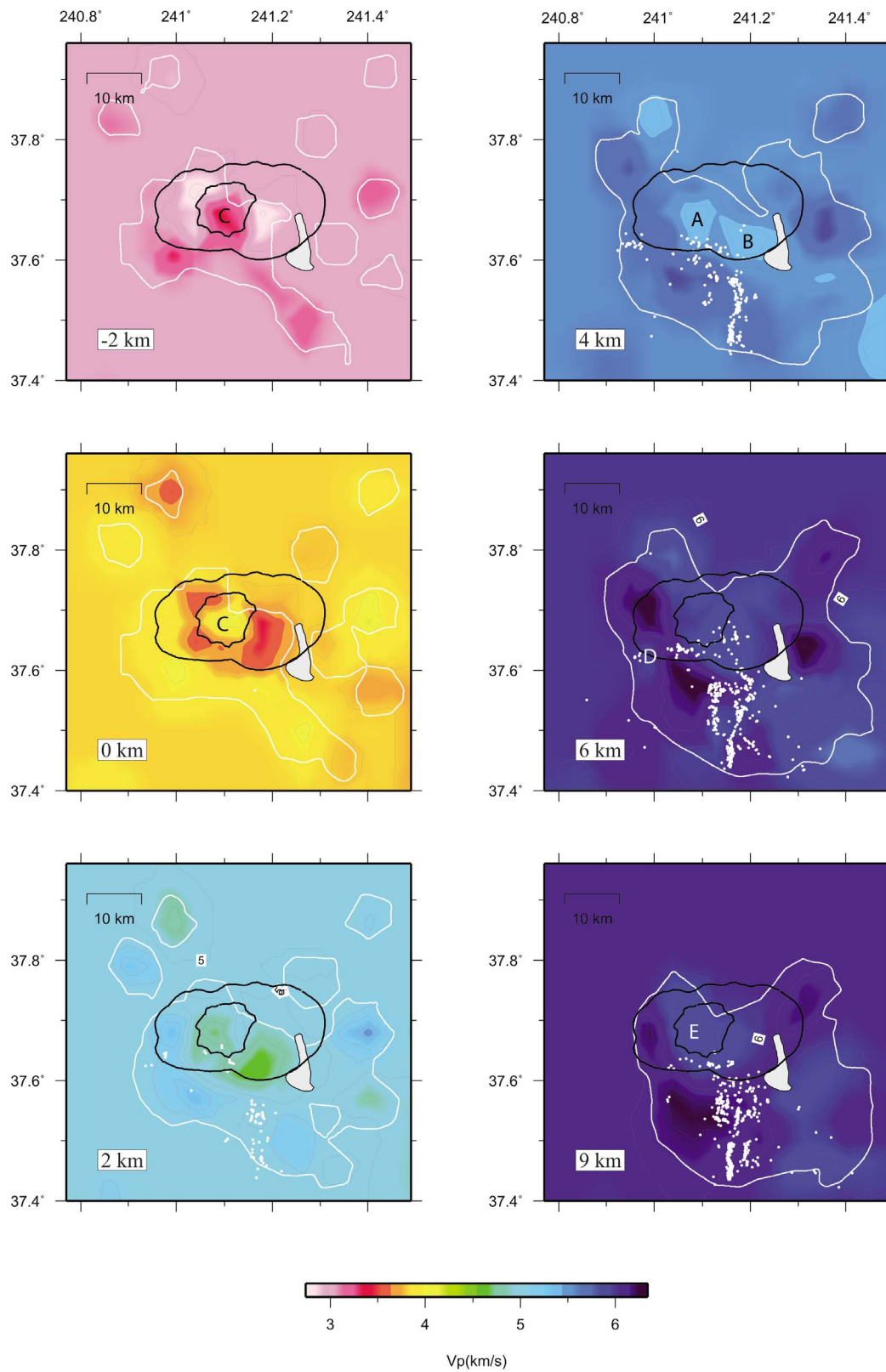


Figure 3. Velocity variations in the inverted layers for model grad-2. The white line outlines the limits of the resolved region where the spread function ≤ 3.0 . In each layer, we plot the relocated seismicity occurring at a depth within 1 km above and below the layer as white dots. A, low- V_p body beneath the resurgent dome; B, low- V_p anomaly beneath Hot Creek Flow; C, high- V_p body beneath the resurgent dome; D, low- V_p anomaly beneath Mammoth Mountain; E, low- V_p anomaly beneath the Long Valley Caldera.

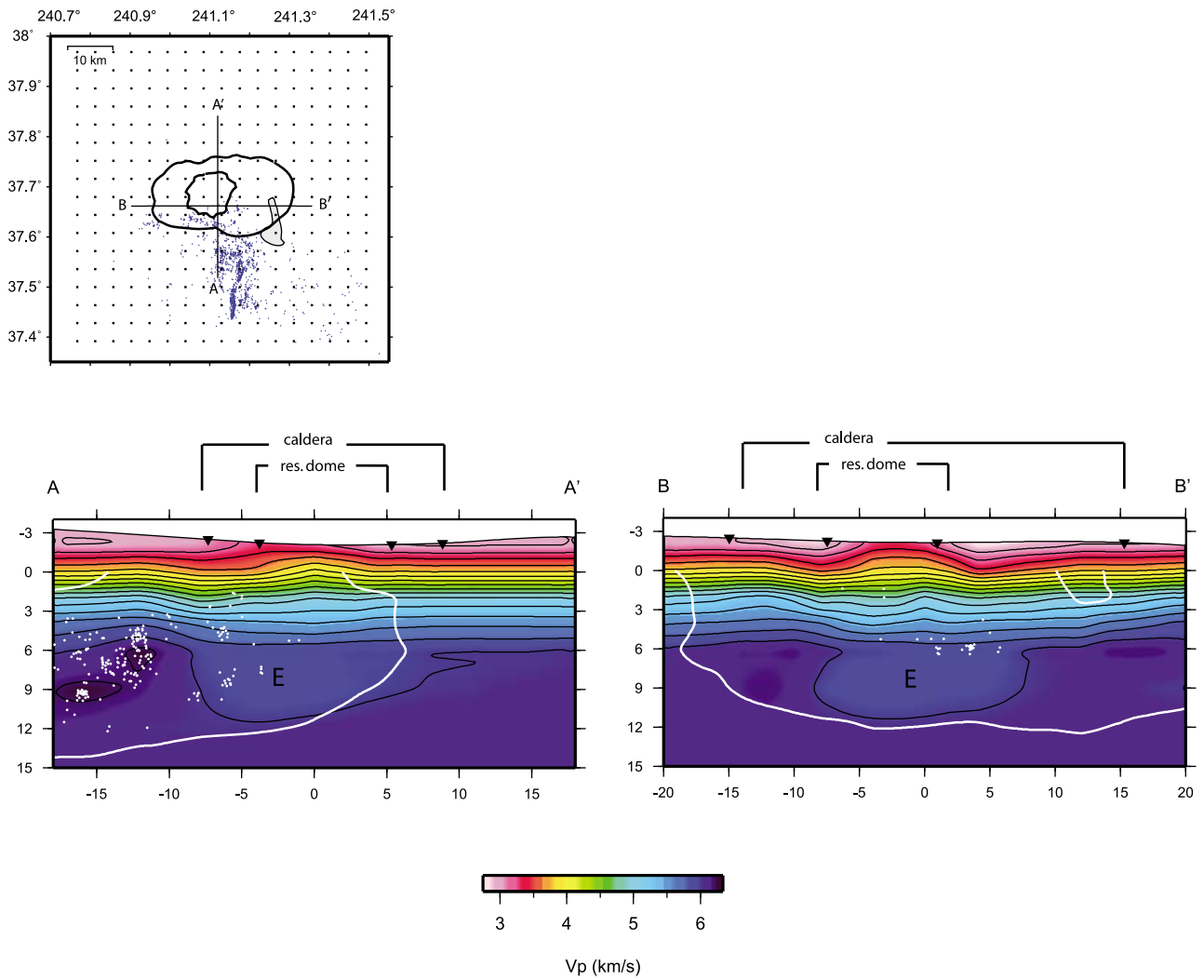


Figure 4. (bottom) Vertical sections of the velocity model grad-2 crossing the caldera and the resurgent dome. White lines indicate the limit of the resolved volume. (top) The earthquakes and grid nodes used in the grad-2 inversion step are shown along with the traces of vertical sections. Label E as in Figure 3.

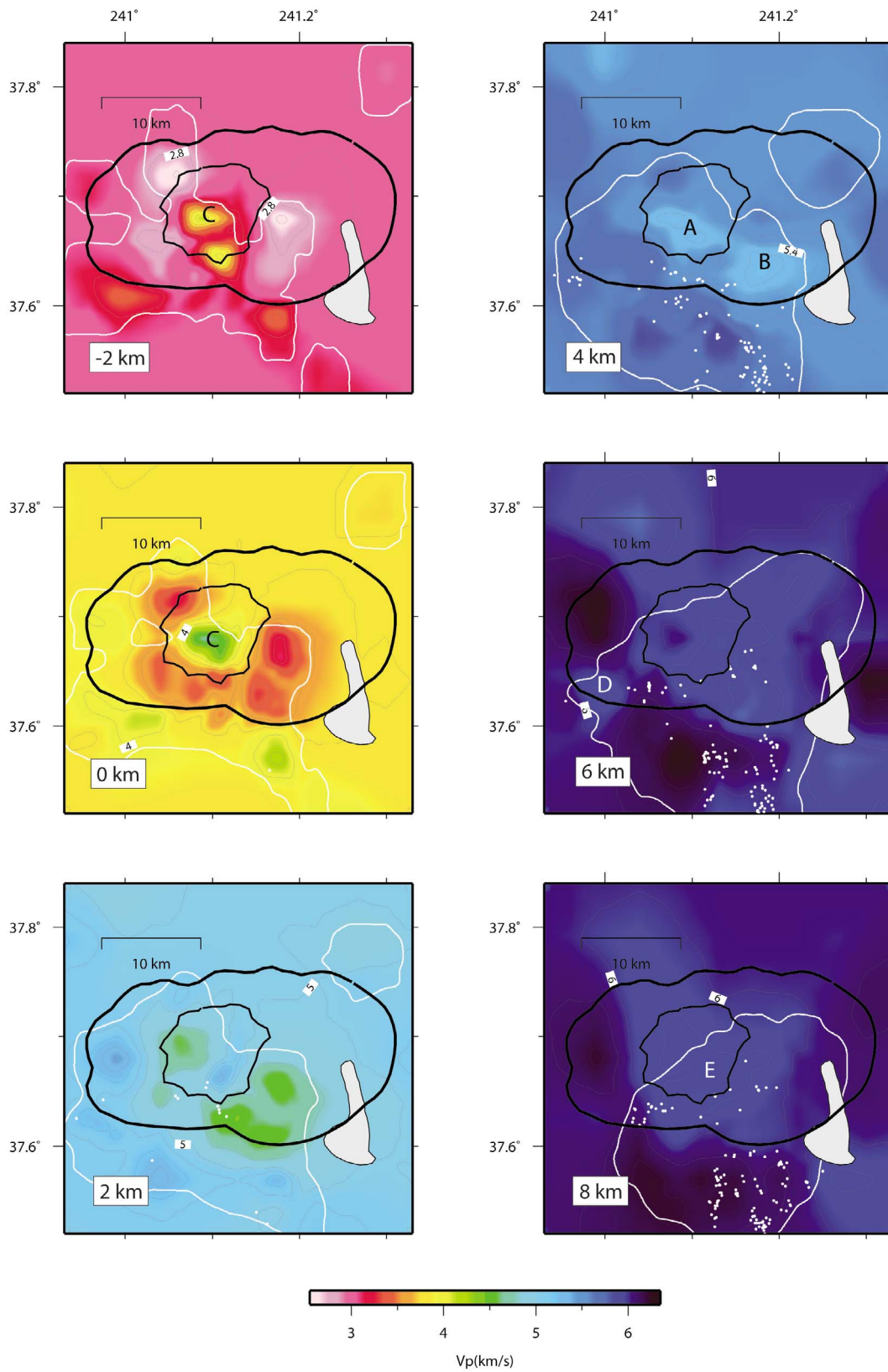


Figure 5. Velocity variations in the inverted layers for model grad-3. The white line outlines the limits of the resolved region where the spread function ≤ 3.0 . In each layer, we plot the relocated seismicity occurring at a depth within 1 km above and below the layer. A, low- V_p body beneath the resurgent dome; B, low- V_p anomaly beneath Hot Creek Flow; C, high- V_p body beneath the resurgent dome; D, low- V_p anomaly beneath Mammoth Mountain; E, low- V_p anomaly beneath the Long Valley Caldera.

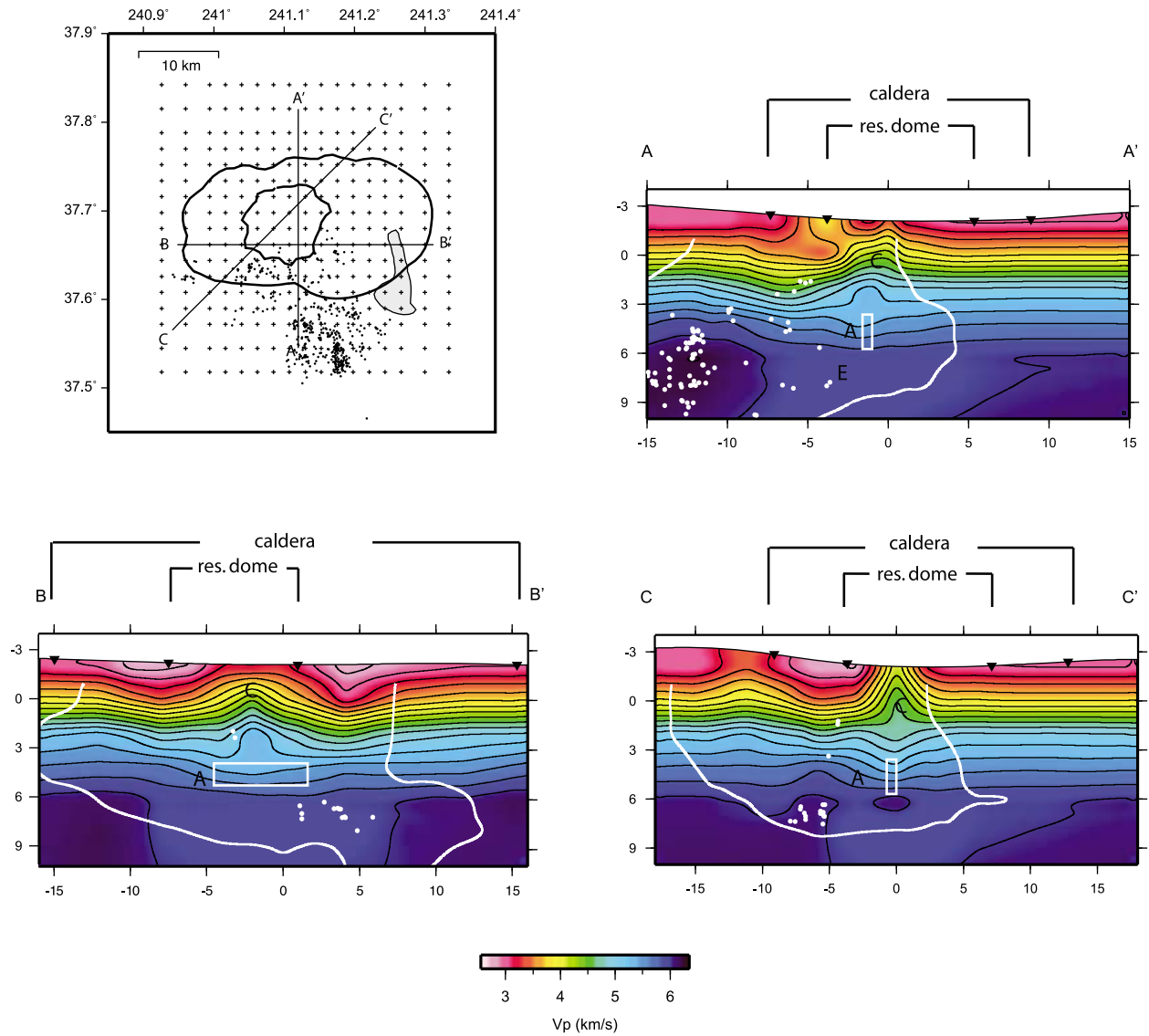


Figure 6. (top right and bottom) Vertical sections of the velocity model grad-3 crossing the caldera and the resurgent dome. White lines indicate the limit of the resolved volume. (top left) The earthquakes and grid nodes used in the grad-3 inversion step are shown along with the traces of vertical sections. Labels A–E as in Figure 5.

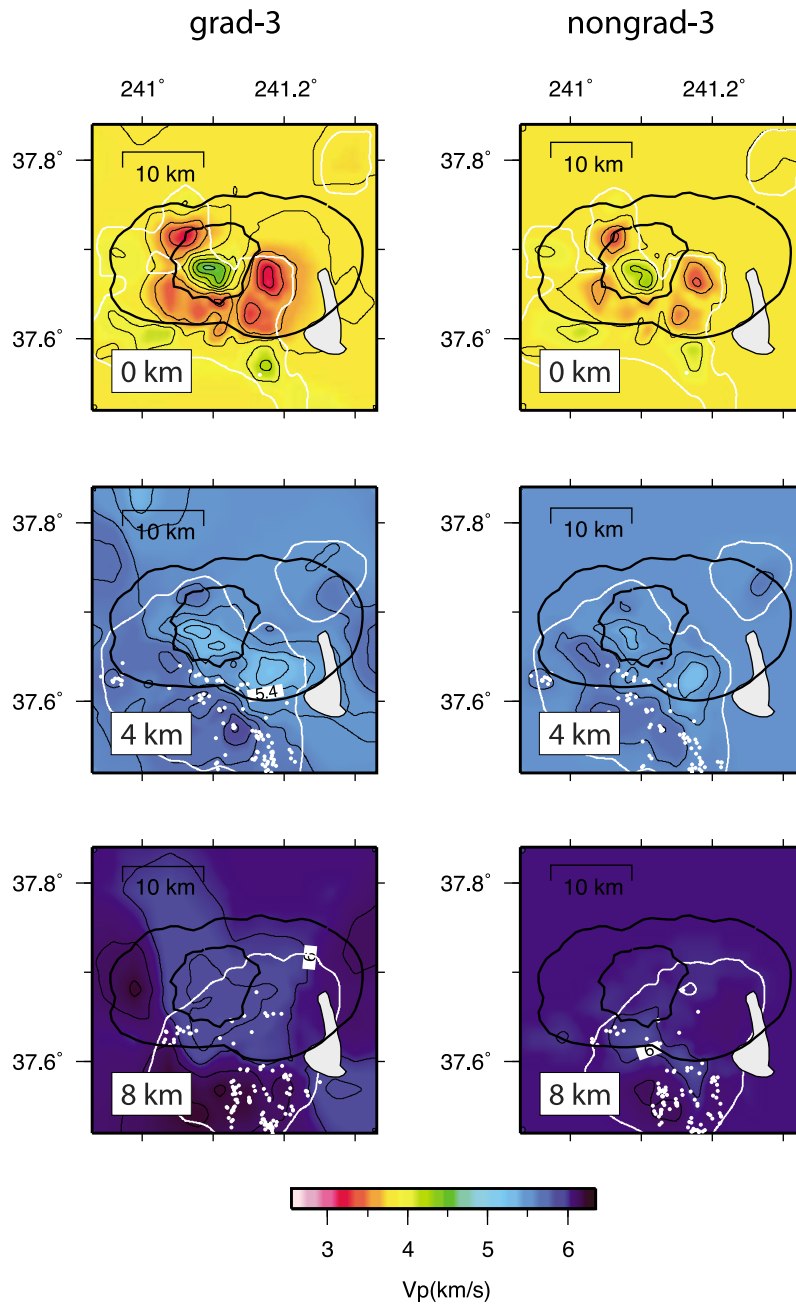


Figure 7. Comparison between grad-3 and nongrad-3 models. The white line outlines the limits of the resolved region where the spread function ≤ 3.0 . In each layer, we plot the relocated seismicity occurring at a depth within 1 km above and below the layer.

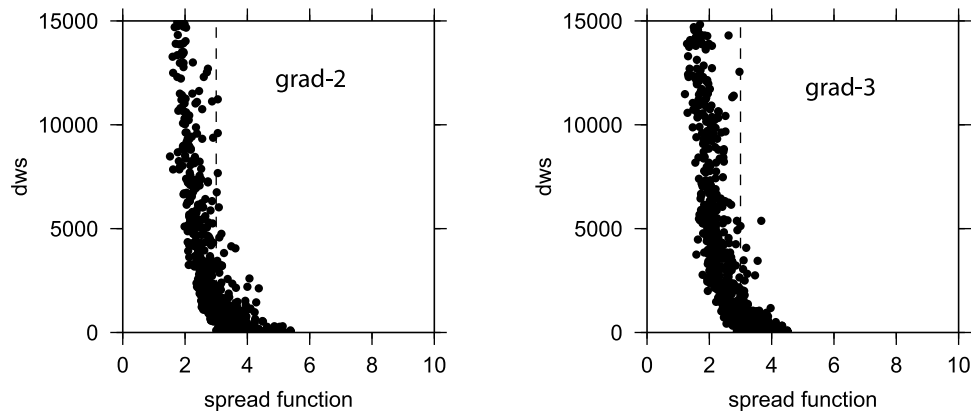


Figure 8. A plot of the DWS versus the spread function (SF) of the averaging vector of the model parameters for grad-2 and grad-3 models. The dashed line at SF = 3.0 is the upper limit of values of the spread function considered to be acceptable (see text for explanation).

is 70% of the diagonal element [Reyners *et al.*, 1999]. Figures 9 and 10 show the 70% smearing contour for nodes with $SF \leq 3$ in the six inverted layers and in W-E trending vertical sections for grad-2. Figures 11 and 12 show the same for grad-3. Well resolved nodes are characterized by low values of SF and smearing effects localized in the surrounding nodes. We found that model parameters with $SF \leq 3$ have good resolution for both models, with only slight smearing of anomalies over adjacent nodes.

[23] We find that the resolution within the caldera is good down to 10 km depth below msl for grad-2 and 8 km below msl for grad-3 (SF values ≤ 3), with the highest resolution in the western, central and southern parts of the caldera.

[24] To further check model resolution we performed a synthetic test in which we simulate the anomaly C with a high- V_p body ($V_p + 10\%$) directly beneath the resurgent dome from the surface elevation to depth of 2 km below msl (synthetic test a). A second synthetic test (synthetic test b) is performed simulating anomaly A, B (at 4 km depth below msl) and E (from 6 to 10 km below msl) as labeled in Figures 3–6, by using a V_p reduction of 5%. Synthetic arrival times are generated, random noise added, and data are inverted using the same parameters as the real inversion.

[25] Synthetic test a shows that the anomaly C is well resolved in the entire volume from surface to 2 km depth below msl. This result reinforces the validity of the V_p model showing that this “spiky” anomaly beneath the dome is not an artifact (Figure 13).

[26] Synthetic test b (Figure 14) shows that the inversion procedure led us to recover an average of ~ 70 – 80% amplitude of the starting model, and a good approximation of the starting geometry. The anomalies A and B are fairly well reproduced as shown in Figure 14. Though we interpret anomaly E primarily by analyzing model grad-2, in which such anomaly is well inside the best resolved volume (Figures 3 and 4), this synthetic test shows that anomaly E is well resolved also in the finer model (grad-3) till the depth of 8 km below msl.

3.2. Teleseismic Receiver Function Results

[27] In this study, we used $M_w \geq 5.5$ teleseismic earthquakes with epicentral distance between 25° and 100°

recorded at three-component stations MLAC and MKV (Figure 15). For MLAC we use 209 teleseisms recorded during the period 2006–2008; for MKV we use 91 teleseisms recorded from 2001 to 2002. The two stations are located inside the caldera at the southeast and west margins of the resurgent dome (Figure 2). Station MLAC is operated by the California Institute of Technology within the Southern California Seismic Network. Station MKV was a temporary installation (1/10/2000 to 26/8/2002) within in the Western Great Basin/Eastern Sierra Nevada network operated by the University of Nevada, Reno. The entire data set for RFs is taken from the IRIS database.

[28] From the data set we select 90 RFs for station MKV and 200 RFs for station MLAC.

[29] The computed RFs for MKV (Figure 16, left) show (1) a strong negative pulse in the 1–2 s time window on radial receiver functions and (2) a high-amplitude signal in the transverse component at 2 s which decreases in amplitude at BAZ 180° – 200° .

[30] Langston and Hammer [2001] identified station MLAC as useless for RF modeling because it has large background noise amplitudes on the T component. We keep a different data set recorded in a later time (2006–2008), which shows large amplitude variations too, but of more minor size than that considered by Langston [2001]. The complex signal in R and T RFs reflects the wave propagation effects associated with the complex 3-D structure of the area. Because of the difficulties already encountered by Langston [2001] in computing and modeling receiver functions for this station, we carefully checked to see if the computed receiver functions contain structures similar to those for MKV.

[31] The main features in the computed RFs for MLAC (Figure 16, right) are (1) a delayed P pulse (at 1–2 s.) on radial receiver functions in 0° – 110° and 280° – 360° BAZ direction followed by a remarkable negative arrival at 3–4 s, (2) a strong negative pulse in 2–3 s time window between 110° and 250° BAZ, and (3) a high-amplitude signal in transverse receiver functions at 2 s which decreases around 180° – 200° BAZ (as for the station MKV).

[32] The computed RF shows complex signals for the two stations for both radial and tangential components.

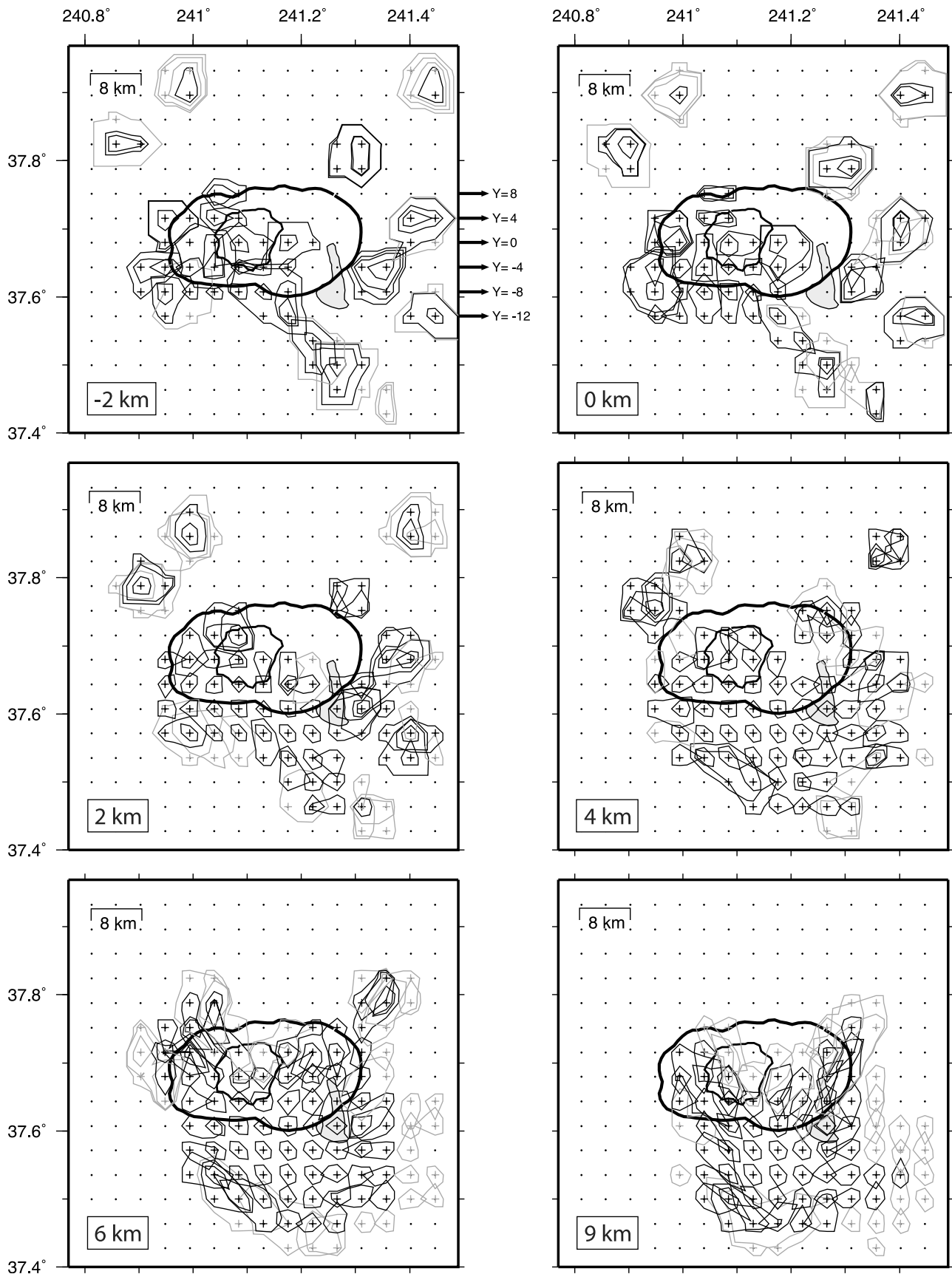


Figure 9

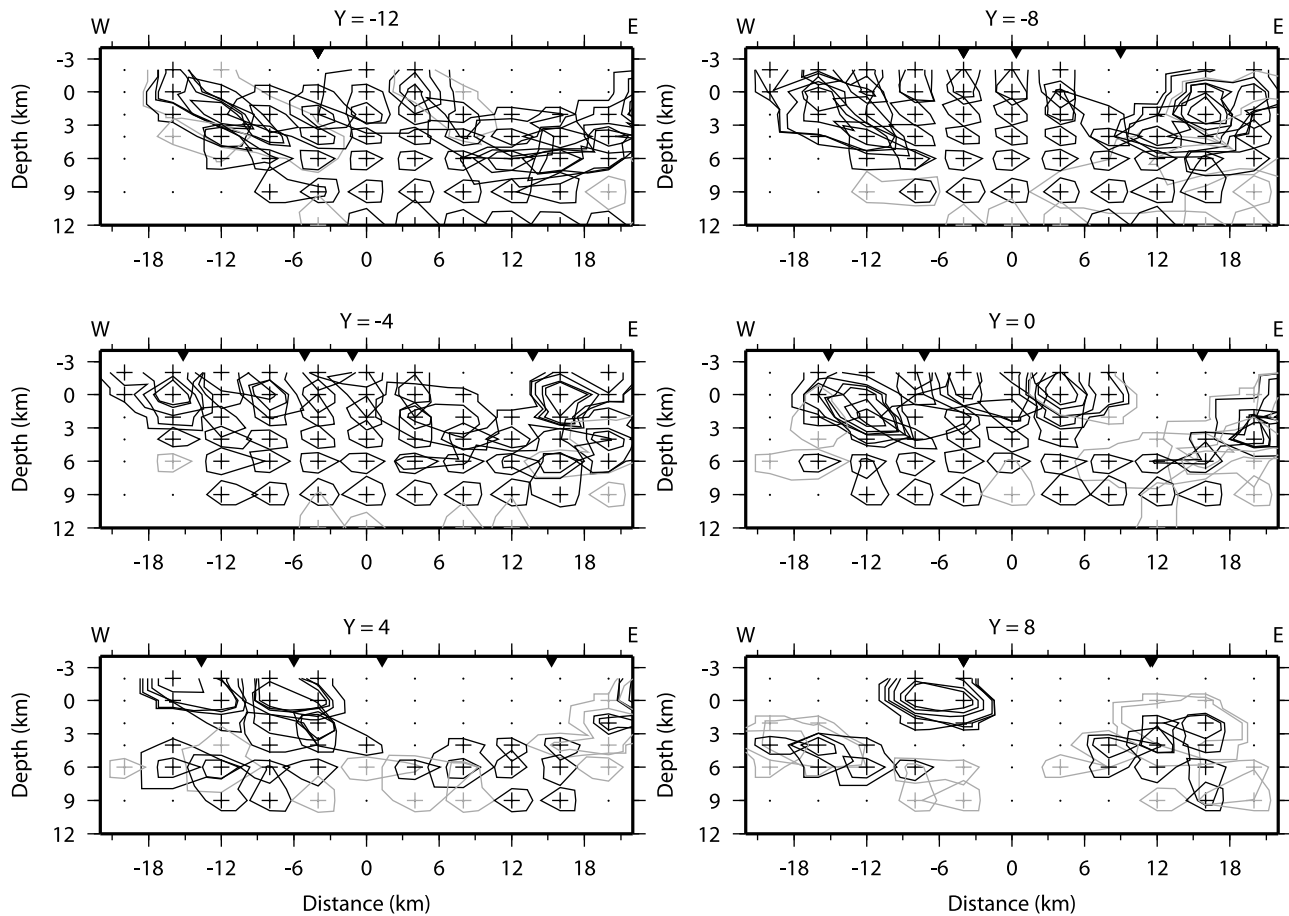


Figure 10. Same as Figure 9 but for six vertical, W-E trending sections.

[33] Figure 17 shows the comparison between computed and synthetic RFs. Our best fit models provide a good fit to both radial and tangential signals, especially the negative pulse in radial component at 2–3 s. for MLAC and the strong negative pulse at 1–2 s. for MKV.

[34] The most notable structure showed by the best fit models is a strong shear wave velocity reduction between 7 and 11 km depth (below msl) for station MKV and between 8 and 10 km depth (below msl) for station MLAC (Figure 18). Such velocity reduction is related to the strong negative pulse in MKV and MLAC RFs radial component in the 1–3 s time window. The best fit models are composed of shallow sub-horizontal interfaces related to caldera fill, while interfaces within the crystalline basement dip northward to northeastward. Such dipping interfaces are probably related to the south moat fault system and were previously recognized by *Prejean et al.* [2002].

[35] The shear wave velocity drop indicated by receiver function inversions is in good agreement with the low- V_p

zone revealed by our tomographic model (Figures 3 and 4), suggesting the presence of a partial melt volume. The continuity of the negative pulse at 1–2 s in the radial component of station MKV, clear from 120° to 330° BAZ (Figure 16), suggests that this signal is plausibly related to a stable 1-D feature, like a diffuse and continuous partial melt volume.

4. Discussion

[36] The use of LET and RFs allows us to describe both shallow and deep structures in the crust beneath Long Valley Caldera. We demonstrate that this approach efficiently resolves previously unrecognized structural details. Using LET, we resolve shallow caldera structures, while teleseismic RFs provide information on deeper structures together with constraints on the interpretation of tomographic models as well as adding new information at greater depth where the resolution of tomographic models is poor.

[37] The main structural details resolved in this study are:

Figure 9. The 70% smearing contouring for inverted nodes (crosses) with spread function (SF) ≤ 3.0 in layers from 0 to 9 km depth for model grad-2. The nodes with SF ≤ 1.5 and with $1.5 < \text{SF} \leq 3.0$ have black and gray crosses and contours, respectively. The black dots indicated the nodes not inverted or the inverted nodes with SF > 3.0 . In the first layer, at –2 km depth, the arrows on the right border indicate the six W-E sections shown in Figure 10. The Y values are the offset distances of the sections from the center of the model.

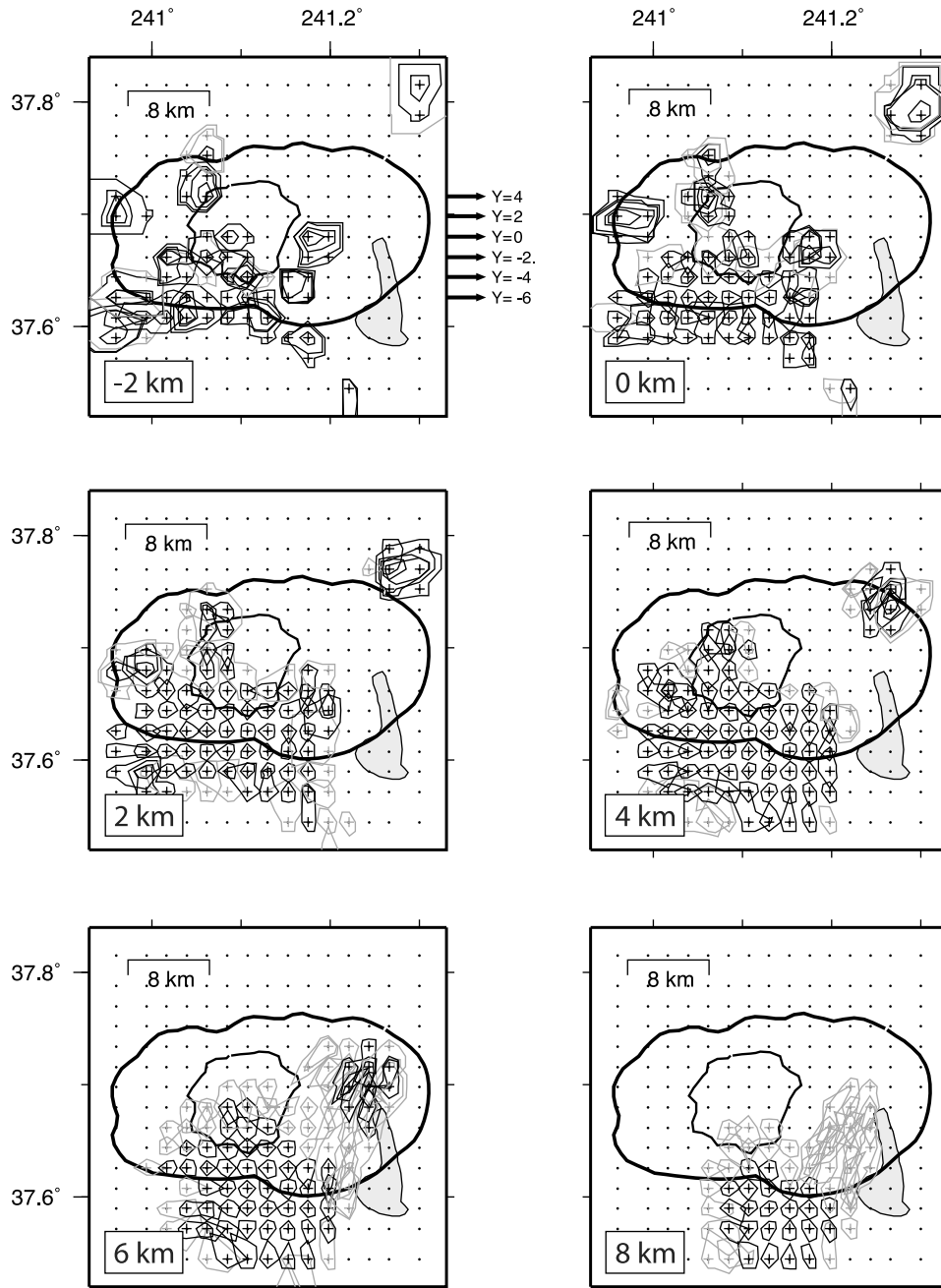


Figure 11. Same as Figure 9 but for model grad-3.

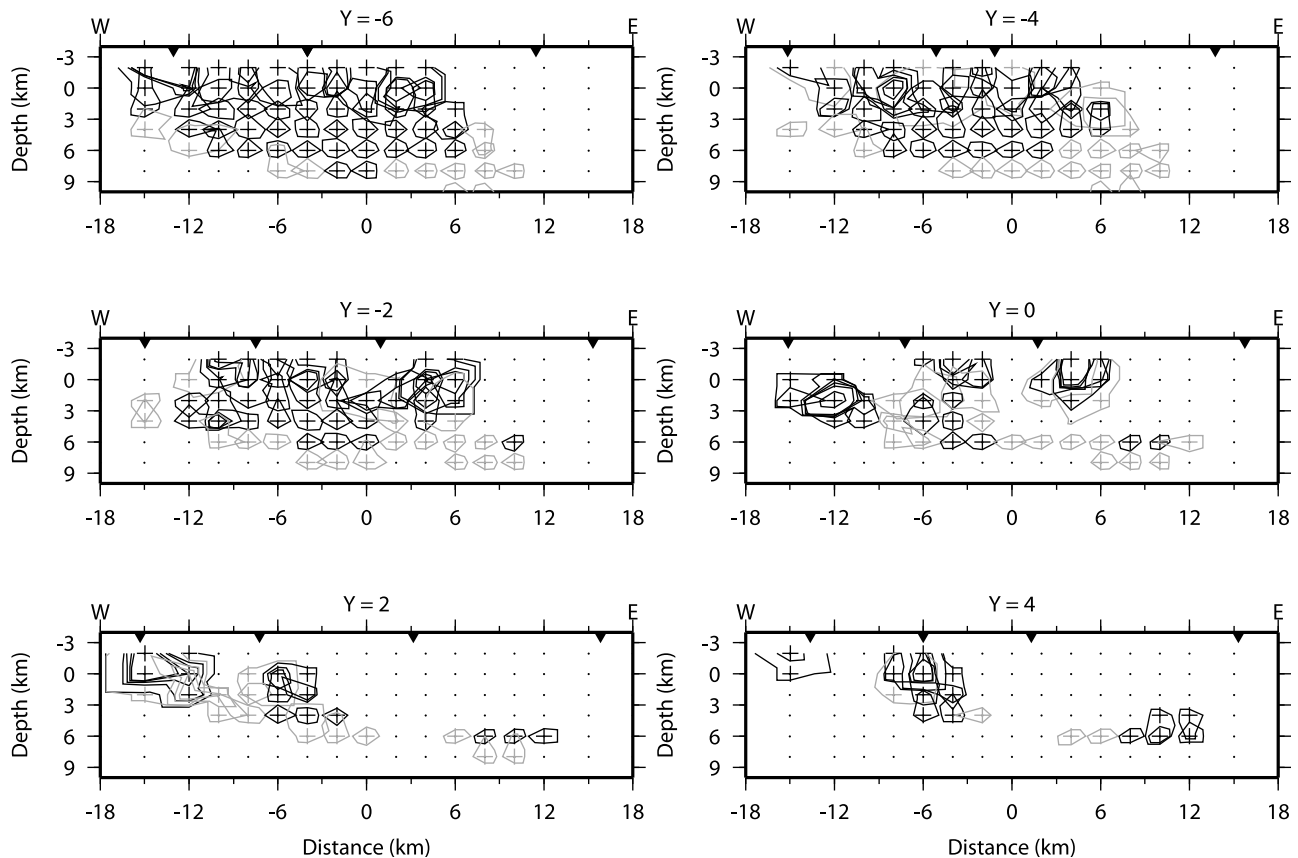


Figure 12. Same as Figure 11 but for six vertical, W-E trending sections of the model grad-3.

[38] 1. An annular zone of low V_p coinciding with post-caldera fill bounding the positive velocity anomaly of the resurgent dome is clearly visible in tomographic models. Postcaldera fill consists of Bishop tuff ash flow deposits, lacustrine sediments, glacial till and landslide deposits. In vertical sections these deposits thin approaching the resurgent dome.

[39] 2. A shallow high- V_p body is present beneath the central-southern section of the resurgent dome, from -1 to 3 km below msl (1 to 5 km below mse), with a lateral extent of ~ 3 km (anomaly C). At the surface, outcrops consist of loose and welded deposits of the postcaldera rhyolitic eruptions, defining eruptive centers eccentric to the dome [Bailey, 1989]. The high- V_p body beneath the resurgent dome may be in part attributed to the intrusion of some rhyolite sills “inflating” the Bishop tuff and in part to up-warping of the underlying crystalline basement.

[40] 3. A WNW trending low- V_p anomaly is centered at a depth of 4 km below msl (6 km below mse), under the southern section of the resurgent dome (anomaly A in Figure 3) at the base of high- V_p body. This low- V_p volume (reduction of about 8 – 10%) coincides with the shallow inflation source modeled by Battaglia *et al.* [2003a] and Langbein [2003]. We hypothesize the presence of an elongated body of partial melt, located beneath the resurgent dome. Relocated earthquakes occur consistently around this body at 4 km depth below msl (Figure 19), supporting its interpretation in term of a hot rock volume hosting partial melt. For silicic volcanic rocks, such

as the rhyolite of Long Valley, a considerable uncertainty remains in linking the observed velocity reductions to the percentage of melt fraction. Studies are limited to dry mafic rocks at mantle conditions, for which Hammond and Humphreys [2000] have shown that a V_p decrease of about 3.6% is compatible with a melt fraction of about 1% . Assuming a similar relation for silicic rocks in the crust, we speculate that the observed velocity reduction represents a melt percentage of about 2 – 3% . The 100°C isothermal temperature in the bottom 1 km (less than 1 km below msl) of the Long Valley Exploratory well, located directly in the center of the resurgent dome (LVEW) (see Sackett *et al.* [1999] for details), and the resistivity in excess of $100 \Omega\text{m}$ to depth of 4 km (~ 1.7 km below msl) suggest that the uppermost resurgent dome is relatively cool and not heated by a proximal magma body [Pribnow *et al.*, 2003; Fischer *et al.*, 2003]. These results do not preclude a recent intrusion of fluids from deeper magmatic sources which cannot yet be detected at the bottom of LVEW (depths of 0 – 1 km below msl), given that the thermal front would take some $10,000$ years to propagate ~ 2 km through rocks with a thermal conductivity of $2.5 \text{ W } ^\circ\text{C}^{-1}\text{m}^{-1}$ above a suddenly intruded sill [Hill, 1992]. The RFs inversions probably cannot resolve such a small structure because the wavelength we analyzed is much larger than the extent of the anomaly revealed by tomographic inversions.

[41] 4. High- V_p anomalies are revealed between 6 km and 8 km below msl beneath the western, southern, and eastern rim of caldera. The increase in V_p with depth within the

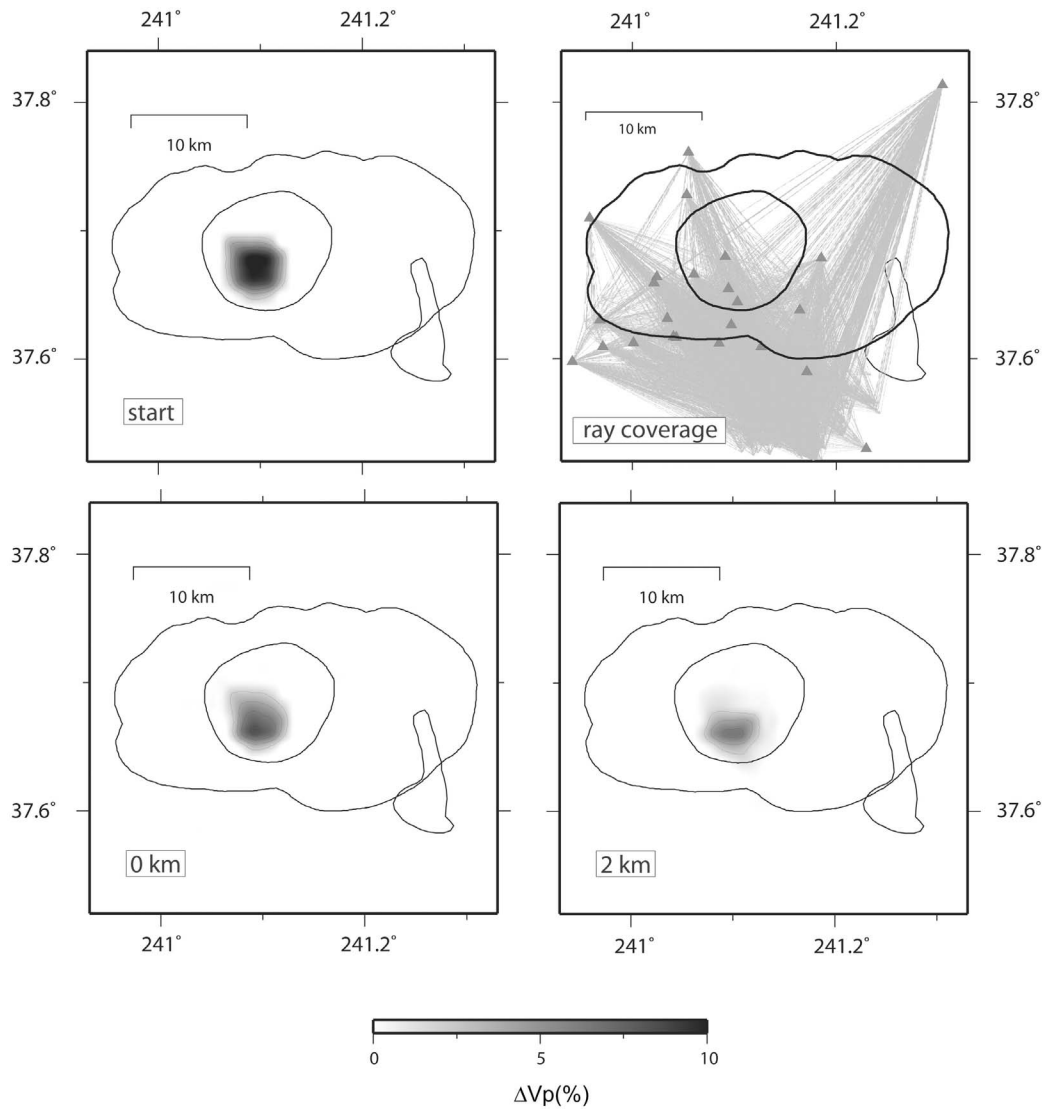


Figure 13. Starting and final model for the synthetic test a. The same synthetic feature is used for three layers, simulating a continuous high- V_p vertical intrusion beneath the resurgent dome (anomaly C in Figures 3–6). The anomaly is well reproduced at depths 0 and 2 km below msl including a decreasing amplitude with depth. We also show raypaths used in the inversion in the top right plot.

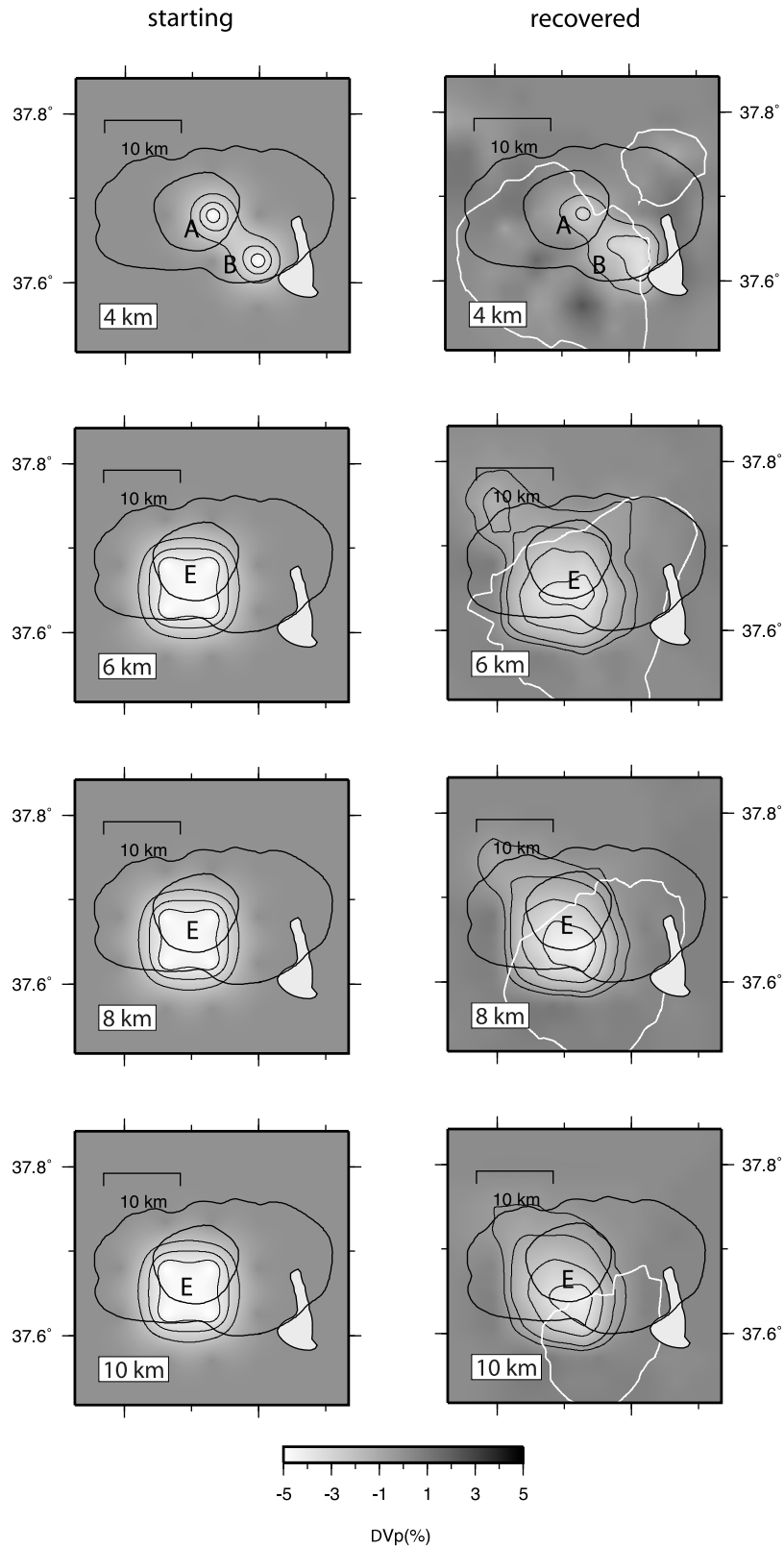


Figure 14. (left) Starting and (right) final models for the synthetic test b. Labels A, B, and E as in Figures 3–6. The three low- V_p anomalies are well reproduced in all layers. Anomaly E is well resolved until the depth of 8 km below msl.

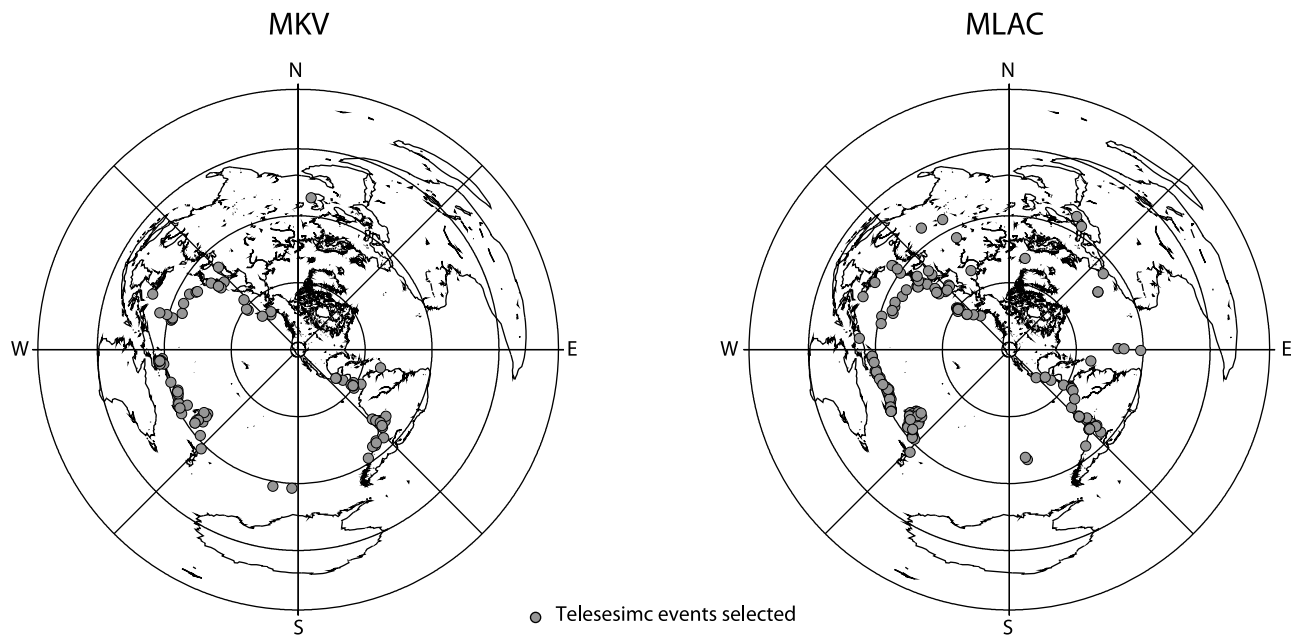


Figure 15. Epicenters for selected teleseismic earthquakes used in the RFs analysis for station (left) MKV and (right) MLAC. Epicenters are indicated by small gray circles.

crystalline basement outside the caldera reflects a typical velocity gradient in crystalline rocks under increasing confining pressure.

[42] 5. A deep, mildly low- V_p anomaly (perturbation around -5%) at depths below 6 km below msl (anomaly E) is located beneath the resurgent dome and the south moat. It is well resolved in both grad-2 and grad-3 tomographic models. This volume coincides with a strong decrease in V_s revealed by the RFs inversion (Figure 18). A similar structure is also resolved in previous tomography studies [e.g., Romero *et al.*, 1993]. Furthermore, deep reflections from the top of such body [Stroujkova and Malin, 2000] provide support for the presence of the deep low- P and low- S wave volume identified in this study. The LET+RFs method leads us to interpret this low-velocity anomaly as due to partial melt volume. According to the laboratory results of Taylor and Singh [2002], the V_s value at 7–11 km depth range below sea level below the station MKV (1 km/s) is compatible with a melt fraction around 40–60%, although the V_p value from tomography (5.6–5.8 km/s) indicates a lesser melt fraction. The drop in V_s at depths of 8–10 km below msl below station MLAC (~ 2 km/s), is consistent with a melt fraction of about 30%.

[43] The results of LET and RFs support the existence of a zone of partial melt in the western portion of south moat in accordance with the location of the top of volumetric deformation source found by Langbein, at 10–18 km below msl. The negative velocity anomaly is bounded by the high V_p of the Sierra crystalline basement, suggesting (Figures 3–6) that the local upwelling of magma was controlled by the regional tectonics. This low-velocity anomaly may represent a residual of a deeper and larger midcrustal magma volume revealed by teleseismic tomography [e.g., Weiland *et al.*, 1995].

[44] The joint analysis and interpretation of receiver functions and tomographic models provides support for a

partial melt volume (inferred by previous tomographic studies [e.g., Weiland *et al.*, 1995]) beneath the southern portion of resurgent dome and south moat at 7–11 km depth below msl (station MKV) thinning toward ESE (station MLAC) (Figure 18). In this region Foulger *et al.* [2004] found evidence of nondouble-couple earthquakes consistent with a combination of tensile and shear faulting and a volume-compensating process. Furthermore the distribution of seismic moment release [Prejean *et al.*, 2002] indicates that the eastern extension of the fault zone is much less active than its western counterpart. Here the seismicity concentrates at a depth of 6 km below msl immediately above the top of the largest, deep low- V_p and low- V_s anomalies (Figure 19). Such seismic sources and their spatial distribution reflect the mutual interaction between tectonics and magmatic system at depth, supporting the idea that ongoing unrest is driven by the regional stress field [Prejean *et al.*, 2002].

[45] The seismicity of the south moat reflects elevated pore pressure driven by hydrous magmatic fluids exolved from the deeper partial melt volume.

[46] The tomographic models, the relocated seismicity, and the receiver function inversions support for the view that the caldera is underlain by a complex magmatic system in which a midcrustal magma body feeds the shallower partial melt volume beneath the resurgent dome through diapiric upwelling or advection beneath the southern margin of the resurgent dome.

5. Conclusions

[47] The tomographic models combined with RFs analysis considerably improve our image of Long Valley Caldera plumbing system.

[48] The enhanced reconstruction of the caldera structure reveals the existence of both negative and positive velocity anomalies that closely match the inferred location and

Q
P
σ_v

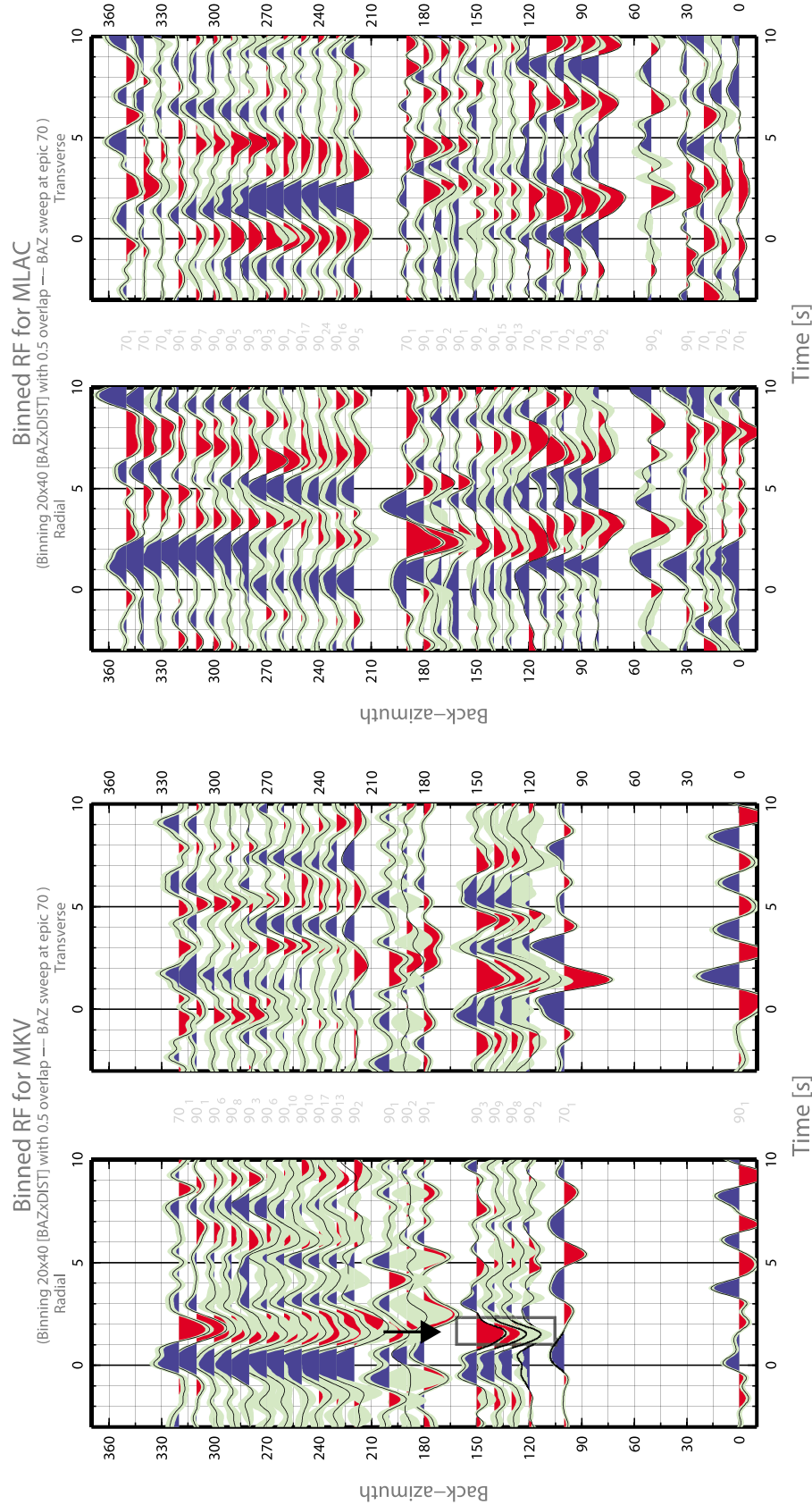


Figure 16. Radial and transverse RFs plotted as a function of BAZ for (left) MKV and (right) MLAC. Earthquakes with epicentral distance between 70° and 100° are included. RFs for MKV show strong negative pulse at 1–2 s in radial component at BAZ 120°–150° (outlined area indicated by arrow).

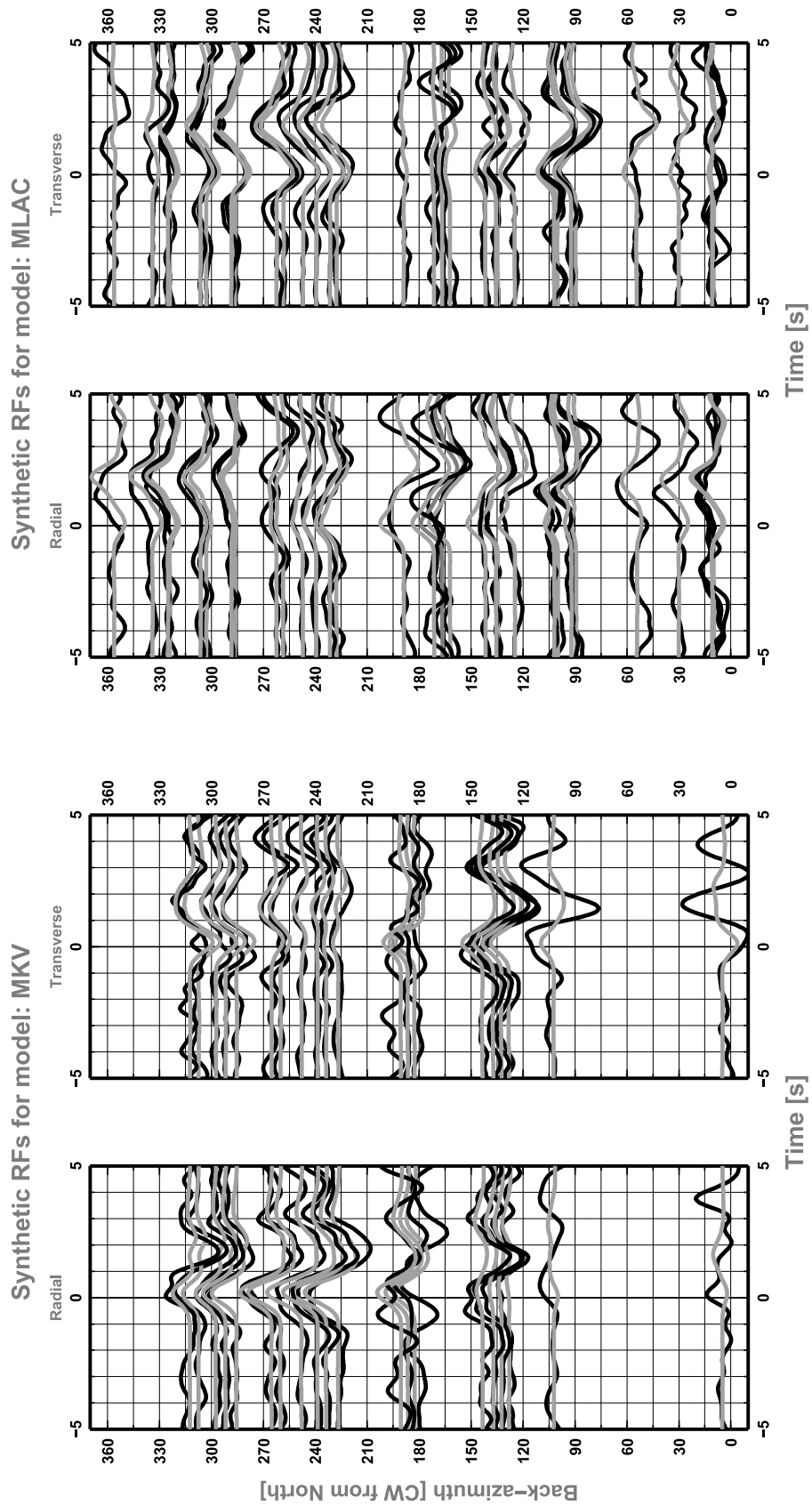


Figure 17. Comparison between computed and synthetic RFs for (left) MKV and (right) MLAC plotted as a function of BAZ. Black lines indicate computed RFs; gray lines are synthetics.

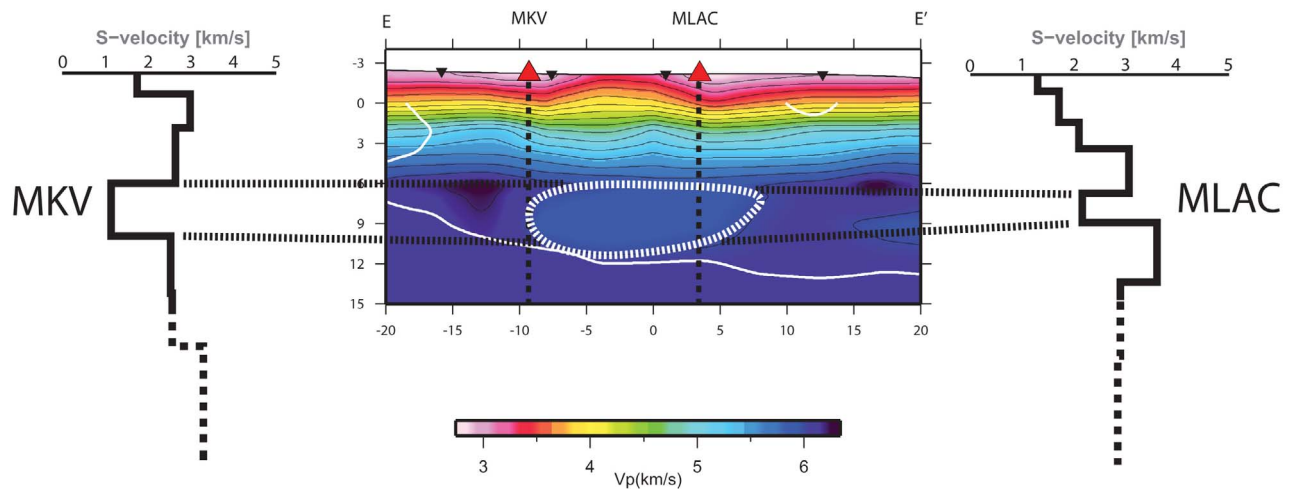


Figure 18. Comparison between tomographic model grad-2 (cross section) and V_s models obtained by receiver functions inversion for stations MKV and MLAC. Cross-section direction is indicated in Figure 2. White solid line in the cross section outlines the resolved region of the tomographic model. White dashed line represents the area interpreted as partial melt.

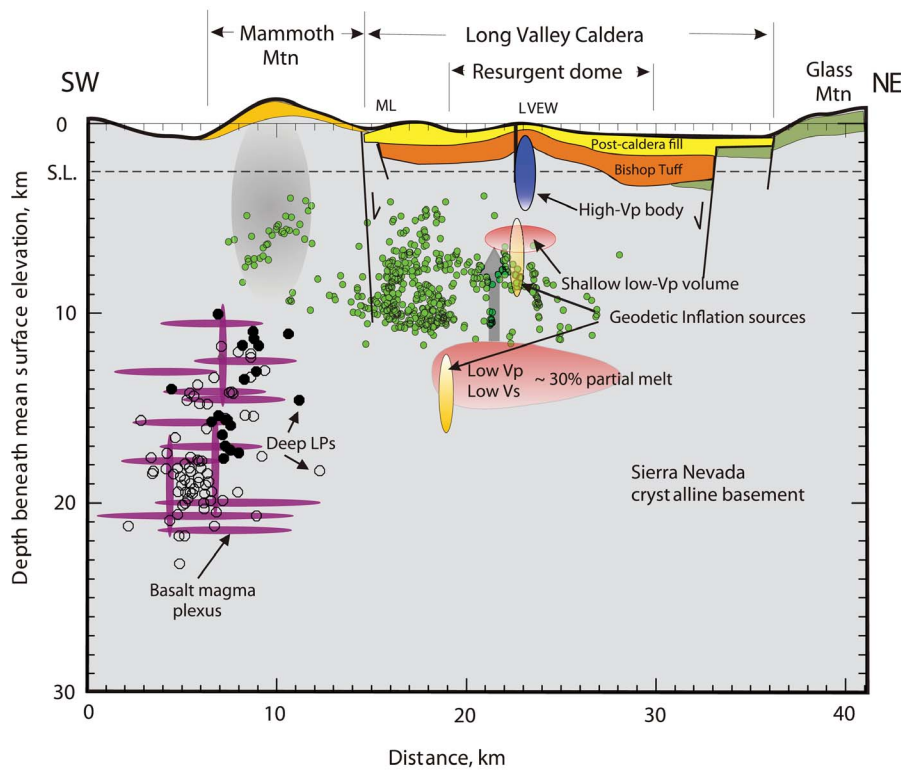


Figure 19. Schematic cross section oriented NE-SW showing the relocated earthquakes and an interpretative sketch of the area. LVEW is the 3 km deep well in the center of the resurgent dome. Small green circles are a selection of earthquakes recorded in the period 1999–2008 relocated with 3-D tomographic model. Large circles are midcrustal long period (LP) earthquakes. Filled circles indicate LP events with hypocenters constrained by a dense seismic network deployed in 1997 [Foulger et al., 1998]. Yellow ellipsoids indicate inflation sources inferred from deformation data [Langbein 2003]. Blue area, high- V_p anomaly beneath the resurgent dome resulting from tomographic inversion; shallow red area, low- V_p anomaly detected by seismic tomography; deep red area, broad low- V_p , low- V_s body inferred from seismic tomography and RFs inversion. Pale gray arrow indicates a likely path for heat flux and mass transport between the deep low-velocity anomaly and the shallow low-velocity anomaly. Modified from Hill [2006, Figure 12].

metry of magma inflation and intrusion inferred from geodetic modeling, and those obtained by teleseismic tomography. At shallow depth, we document the up-warping of both the Bishop Tuff and the crystalline basement due to the intrusion of multiple rhyolite sills beneath the central-southern section of the resurgent dome. An elongated low- V_p anomaly at 4–5 km below msl (or 6–7 km below mse) is evidence for hot rock hosting a partial melt volume. Although the estimate of the amount of melt is speculative, the V_p reduction may indicate 2–3 % of melt. Its position is almost coincident with the inferred inflation source. Our study supports the model of magma intrusion proposed by Tizzani *et al.* [2009].

[49] A broad, low- V_p volume at depths greater than 6 km (below msl) represents the upper portion of the larger, mid-crustal low-velocity volume suggested by previous teleseismic studies [Dawson *et al.*, 1990; Weiland, 1995]. This anomaly is supported by V_s models obtained by RFs inversions for stations MKV and MLAC, which show a strong V_s reduction at about 7–11 km depth. Such an anomaly is consistent with the presence of an extensive, partial-melt volume that may be related to the residual Bishop magma chamber. The melt percentage for the V_s values obtained by RFs inversion, according to Taylor and Singh [2002], is in the range of 30–60%. Its lateral extent, bounded on west and south by the regional Sierra faults and the south moat faults, respectively, suggests a strong interaction between magmatic and tectonic processes.

[50] We hypothesize an interaction between the deep and shallow low- V_p bodies. The partial melt volume at 4–5 km below msl is plausibly fed by the deep magma body through the diapiric upwelling beneath the southern margin of the resurgent dome (Figure 19).

[51] **Acknowledgments.** We are grateful to Phil Dawson and Bruce Julian for their constructive reviews of an early draft of this paper. Nicola Piana Agostinetti provided receiver function analysis codes. We thank the Associate Editor and two anonymous reviewers for providing very useful suggestions to improve the manuscript. Materials provided by the IRIS Education and Outreach Program have been used in this study. The facilities of the IRIS Data Management System, and specifically the IRIS Data Management Center, were used for access to waveform and metadata required in this study. The IRIS DMS is funded through the National Science Foundation and specifically the GEO Directorate through the Instrumentation and Facilities Program of the National Science Foundation under Cooperative Agreement EAR-0552316. GMT [Wessel and Smith, 1991] was used for developing figures.

References

- Bailey, R. A. (1976) On the mechanisms of postsubsidence central doming and volcanism in resurgent cauldrons, *Geol. Soc. Am. Abstr. Programs*, 8(5), 567.
- Bailey, R. C. (1989), Geologic map of Long Valley Caldera, Mono-Inyo Craters volcanic chain, and vicinity, eastern California, *U.S. Geological Survey, Miscellaneous Investigations Series Map I-1933*, scale 1:62,500.
- Battaglia, M., C. Roberts, and P. Segall (1999), Magma intrusion beneath Long Valley Caldera confirmed by temporal changes in gravity, *Science*, 285, 2119–2122, doi:10.1126/science.285.5436.2119.
- Battaglia, M., P. Segall, J. Murray, P. Cervelli, and J. Langbein (2003a), The mechanics of unrest at Long Valley Caldera, California: 1. Modeling the geometry of the source using GPS, leveling and 2-color EDM data, *J. Volcanol. Geotherm. Res.*, 127, 195–217, doi:10.1016/S0377-0273(03)00170-7.
- Battaglia, M., P. Segall, and C. Roberts (2003b), The mechanics of unrest at Long Valley Caldera, California: 2. Constraining the nature of the source using geodetic and micro-gravity data, *J. Volcanol. Geotherm. Res.*, 127, 219–245, doi:10.1016/S0377-0273(03)00171-9.

- Benz, H. M., B. A. Chouet, P. B. Dawson, J. C. Lahr, R. A. Page, and J. A. Hole (1996), Three-dimensional P and S wave velocity structure of Redoubt Volcano, Alaska, *J. Geophys. Res.*, 101, 8111–8128, doi:10.1029/95JB03046.
- Chiarabba, C., and M. Moretti (2006), An insight into the unrest phenomena at the Campi Flegrei Caldera from V_p and V_p/V_s tomography, *Terra Nova*, 18(6), 373–379, doi:10.1111/j.1365-3121.2006.00701.x.
- Chiarabba, C., J. R. Evans, and A. Amato (1995), Variations on the NeHT high-resolution tomography method: A test of technique and results for Medicine Lake Volcano, northern California, *J. Geophys. Res.*, 100, 4035–4052, doi:10.1029/94JB02771.
- Chiarabba, C., A. Amato, E. Boschi, and F. Barberi (2000), Recent seismicity and tomographic modeling of the Mt. Etna plumbing system, *J. Geophys. Res.*, 105, 10,923–10,938, doi:10.1029/1999JB900427.
- Chmielowski, J., G. Zandt, and C. Haberland (1999), The central Andean Altopiano-Puna magma body, *Geophys. Res. Lett.*, 26(6), 783–786, doi:10.1029/1999GL900078.
- Darbyshire, F. A., K. F. Priestley, R. S. White, R. Stefansson, G. B. Gudmundsson, and S. S. Jakobsdottir (2000), Crustal structure of central and northern Iceland from analysis of teleseismic receiver functions, *Geophys. J. Int.*, 143, 163–184, doi:10.1046/j.1365-246x.2000.00224.x.
- Dawson, P. B., J. R. Evans, and H. M. Iyer (1990), Teleseismic tomography of the compressional wave velocity structure beneath the Long Valley region, California, *J. Geophys. Res.*, 95(7), 11,021–11,050.
- De Gori, P., C. Chiarabba, and D. Patanè (2005), Qp structure of Mt. Etna: Constraints for the physics of the plumbing system, *J. Geophys. Res.*, 110, B05303, doi:10.1029/2003JB002875.
- Di Bona, M. (1998), Variance estimate in frequency-domain deconvolution for teleseismic receiver function computation, *Geophys. J. Int.*, 134, 634–646, doi:10.1111/j.1365-246X.1998.tb07128.x.
- Di Stefano, R., and C. Chiarabba (2002), Active source tomography at Mt. Vesuvius: Constraints for the magmatic system, *J. Geophys. Res.*, 107(B11), 2278, doi:10.1029/2001JB000792.
- Eberhart-Phillips, D. (1990), Three-dimensional velocity structure in the Coalinga region, California, *J. Geophys. Res.*, 95, 15,343–15,363, doi:10.1029/JB095iB10p15343.
- Eberhart-Phillips, D. (1993), Local earthquake tomography: Earthquake source regions, in *Seismic Tomography: Theory and Practice*, edited by H. M. Iyer and K. Hirahara, pp. 613–643, Chapman and Hall, New York.
- Eberhart-Phillips, D., and M. Reyners (1997), Continental subduction and three dimensional crustal structure: The northern South Island, New Zealand, *J. Geophys. Res.*, 102, 11,843–11,861, doi:10.1029/96JB03555.
- Ellsworth, W. L., and R. Y. Koyanagi (1977), Three-dimensional crust and mantle structure of Kilauea volcano, *J. Geophys. Res.*, 82, 5379–5394, doi:10.1029/JB082i033p05379.
- Evans, J. R., and J. J. Zucca (1993), Active-source high resolution (NeHT) tomography: Velocity and Q , in *Seismic Tomography: Theory and Practice*, edited by H. M. Iyer and K. Hirahara, pp. 695–732, Chapman and Hall, New York.
- Fischer, M., K. Roller, M. Kuster, B. Stockhert, and V. S. McConnell (2003), Open fissure mineralization at 2600 m depth in Long Valley Exploratory Well (California)—Insight into history of the hydrothermal system, *J. Volcanol. Geotherm. Res.*, 127, 347–363, doi:10.1016/S0377-0273(03)00176-8.
- Foulger, G. R., B. R. Julian, A. M. Pitt, and D. P. Hill (2003) Three-dimensional crustal structure of Long Valley Caldera, California, and evidence for the migration of CO_2 under Mammoth Mountain, *J. Geophys. Res.*, 108(B3), 2147, doi:10.1029/2000JB000041.
- Foulger, G. R., B. R. Julian, D. P. Hill, A. M. Pitt, P. E. Malin, and E. Shalev (2004), Non-double-couple microearthquakes at Long Valley Caldera, California, provide evidence for hydraulic fracturing, *J. Volcanol. Geotherm. Res.*, 132, 45–71, doi:10.1016/S0377-0273(03)00420-7.
- Frederiksen, A. W., and M. G. Bostock (2000), Modeling teleseismic waves in dipping anisotropic structures, *Geophys. J. Int.*, 141, 401–412, doi:10.1046/j.1365-246x.2000.00090.x.
- Hammond, W. C., and E. D. Humphreys (2000), Upper mantle seismic wave velocity: Effects of realistic partial melt geometries, *J. Geophys. Res.*, 105, 10,975–10,986, doi:10.1029/2000JB900041.
- Hildreth, W. (2004), Volcanological perspectives on Long Valley, Mammoth Mountain, and Mono Craters: Several contiguous but discrete systems, *J. Volcanol. Geotherm. Res.*, 136, 169–198, doi:10.1016/j.jvolgeores.2004.05.019.
- Hill, D. P. (1976), Structure of Long Valley Caldera, California, from a seismic refraction experiment, *J. Geophys. Res.*, 81(5), 745–753, doi:10.1029/JB081i005p00745.
- Hill, D. P. (1992), Temperatures at the base of the seismogenic crust beneath Long Valley Caldera, California, and the Phlegrean Fields

- Caldera, Italy, in *Volcanic Seismology*, edited by P. Gasparini and R. Scarpa, pp. 431–460, Springer, Berlin.
- Hill, D. P. (2006), Unrest in Long Valley Caldera, California, 1978–2004, *Geol. Soc. Spec. Publ.*, 269, 1–24, doi:10.1144/GSL.SP.2006.269.01.02.
- Hill, D. P., and S. Prejean (2005), Volcanic unrest beneath Mammoth Mountain, California, *J. Volcanol. Geotherm. Res.*, 146, 257–283, doi:10.1016/j.jvolgeores.2005.03.002.
- Iyer, H. M., J. R. Evans, P. B. Dawson, D. A. Stauber, and U. Achauer (1990), Differences in magma storage in different volcanic environments as revealed by seismic tomography: Silicic volcanic center and subduction-related volcanoes, in *Magma Transport and Storage*, edited by M. P. Ryan, John Wiley, Chichester, U. K.
- Kissling, E. (1988), Geotomography with local earthquake data, *Rev. Geophys.*, 26, 659–698, doi:10.1029/RG026i004p00659.
- Lahr, J. C. (1989), HYPOELLIPSE/version 2.00: A computer program for determining local earthquake hypocentral parameters, magnitude and first motion pattern, *U.S. Geol. Surv. Open File Rep.*, 89-16, 162 pp.
- Langbein, J. O. (2003), Deformation of the Long Valley Caldera, California: Inferences from measurements from 1988 to 2001, *J. Volcanol. Geotherm. Res.*, 127, 247–267, doi:10.1016/S0377-0273(03)00172-0.
- Langbein, J. O., D. P. Hill, T. N. Parker, and S. K. Wilkinson (1993), An episode of reinflation of Long Valley Caldera, eastern California: 1989–1991, *J. Geophys. Res.*, 98(B9), 15,851–15,870, doi:10.1029/93JB00558.
- Langston, C. A. (1979), Structure under Mount Rainier, Washington, inferred from teleseismic body waves, *J. Geophys. Res.*, 84, 4749–4762, doi:10.1029/JB084iB09p04749.
- Langston, C. A., and J. K. Hammer (2001), The vertical component *P* wave receiver function, *Bull. Seism. Soc. Am.*, 91, 1091–1106.
- Lees, J. M. (1992), The magma system of Mount St. Helens: Non linear high resolution *P* wave tomography, *J. Volcanol. Geotherm. Res.*, 53, 103–116, doi:10.1016/0377-0273(92)90077-Q.
- Mavko, G. M. (1980), Velocity and attenuation in partially molten rocks, *J. Geophys. Res.*, 85, 5173–5189, doi:10.1029/JB085iB10p05173.
- Michellini, A., and T. V. McEvilly (1991), Seismological studies at Parkfield. I. Simultaneous inversion for velocity structure and hypocenters using cubic B-splines parameterization, *Bull. Seismol. Soc. Am.*, 81, 524–552.
- Mori, J., D. Eberhart-Phillips, and D. Harlow (1996), Three-dimensional velocity structure at Mount Pinatubo: Resolving magma bodies and earthquake hypocenters, in *Fire and Mud, Eruptions and Lahars of Mount Pinatubo, Philippines*, edited by C. G. Newhall and R. S. Punoungbayan, pp. 371–382, Univ. of Wash. Press, Seattle.
- Nakamichi, H., S. Tanaka, and H. Hamaguchi (2002), Fine *S* wave velocity structure beneath Iwate volcano, northeastern Japan, as derived from receiver functions and travel times, *J. Volcanol. Geotherm. Res.*, 116, 235–255, doi:10.1016/S0377-0273(02)00218-4.
- O’Connell, R. J., and B. Budiansky (1977), Viscoelastic properties of fluid-saturated cracked solids, *J. Geophys. Res.*, 82, 5719–5736, doi:10.1029/JB082i036p05719.
- Park, J., H. Yuan, and V. Levin (2004), Subduction zone anisotropy beneath Corvallis, Oregon: A serpentinite skid mark of trench-parallel terrane migration? *J. Geophys. Res.*, 109, B10306, doi:10.1029/2003JB002718.
- Piana Agostinetti, N., and C. Chiarabba (2008), Seismic structure beneath Mt. Vesuvius from receiver function analysis and local earthquakes tomography: Evidences for location and geometry of the magma chamber, *Geophys. J. Int.*, 175(3), 1298–1308, doi:10.1111/j.1365-246X.2008.03868.x.
- Ponko, S. C., and C. O. Sanders (1994), Inversion for *P* and *S* wave attenuation structure, Long Valley Caldera, California, *J. Geophys. Res.*, 99(B2), 2619–2635, doi:10.1029/93JB03405.
- Prejean, S., W. Ellsworth, M. Zoback, and F. Walhouser (2002), Fault structure and kinematics of the Long Valley Caldera region, California, revealed by high-accuracy earthquake hypocenters and focal mechanism stress inversions, *J. Geophys. Res.*, 107(B12), 2355, doi:10.1029/2001JB001168.
- Prejean, S., A. Stork, W. Ellsworth, D. Hill, and B. Julian (2003), High precision earthquake locations reveal seismogenic structure beneath Mammoth Mountain, CA in 1989, *Geophys. Res. Lett.*, 30(24), 2247, doi:10.1029/2003GL018334.
- Pribnow, D. F. C., C. Schutze, S. J. Hurter, C. Flechsig, and J. H. Sasse (2003), Fluid flow in the resurgent dome of Long Valley Caldera: Implications from thermal data and deep electrical sounding, *J. Volcanol. Geotherm. Res.*, 127, 329–345, doi:10.1016/S0377-0273(03)00175-6.
- Reyners, M., D. Eberhart-Phillips, and G. Stuart (1999), A three-dimensional image of shallow subduction: Crustal structure of the Raukumara Peninsula, New Zealand, *Geophys. J. Int.*, 137, 873–890, doi:10.1046/j.1365-246x.1999.00842.x.
- Romero, A. E., Jr., T. V. McEvilly, E. L. Majer, and A. Michellini (1993), Velocity structure of the Long Valley Caldera from the inversion of local earthquake *P* and *S* travel times, *J. Geophys. Res.*, 98(B11), 19,869–19,879, doi:10.1029/93JB01553.
- Sackett, P. C., V. S. McConnell, A. L. Roach, S. S. Priest, and J. H. Sasse (1999), Long Valley Coring Project, Inyo County, 1998—Preliminary stratigraphy and images of recovered core, *U.S. Geol. Surv. Open File Rep.*, 99-158.
- Sambridge, M. (1999a), Geophysical inversion with a neighbourhood algorithm—I. Searching a parameter space, *Geophys. J. Int.*, 138, 479–494, doi:10.1046/j.1365-246X.1999.00876.x.
- Sambridge, M. (1999b), Geophysical inversion with a neighbourhood algorithm—II. Appraising the ensemble, *Geophys. J. Int.*, 138, 727–746, doi:10.1046/j.1365-246x.1999.00900.x.
- Sanders, C. O., S. C. Ponko, L. D. Nixon, and E. A. Schwartz (1995), Seismological evidence for magmatic and hydrothermal structure in Long Valley Caldera from local earthquake attenuation and velocity tomography, *J. Geophys. Res.*, 100(B5), 8311–8326, doi:10.1029/95JB00152.
- Sato, H., I. S. Sacks, and T. Murase (1989), The use of laboratory velocity data for estimating temperature and partial melt fraction in the low-velocity zone: Comparison with heat flow and electrical conductivity studies, *J. Geophys. Res.*, 94, 5689–5704, doi:10.1029/JB094iB05p05689.
- Steck, L., and W. A. Prothero (1994), Crustal structure beneath Long Valley Caldera from modeling of teleseismic *P* wave polarizations and *Ps* converted phases, *J. Geophys. Res.*, 99, 6881–6898, doi:10.1029/93JB03284.
- Stroujkova, A. F., and P. E. Malin (2000), A magma mass beneath Casa Diablo? Further evidence from reflected seismic waves, *Bull. Seismol. Soc. Am.*, 90(2), 500–511, doi:10.1785/0119990071.
- Taylor, M. A. J., and S. C. Singh (2002), Composition and microstructure of magma bodies from effective medium theory, *Geophys. J. Int.*, 149, 15–21, doi:10.1046/j.1365-246X.2002.01577.x.
- Thurber, C. H. (1983), Earthquake locations and three-dimensional crustal structure in the Coyote Lake area, central California, *J. Geophys. Res.*, 88, 8226–8236, doi:10.1029/JB088iB10p08226.
- Thurber, C. H. (1984), Seismic detection of the summit magma complex of Kilauea volcano, Hawaii, *Science*, 223, 165–167, doi:10.1126/science.223.4632.165.
- Tizzani, P., M. Battaglia, G. Zeni, S. Atzori, P. Berardino, and R. Lanari (2009), Uplift and magma intrusion at Long Valley Caldera from InSAR and gravity measurements, *Geology*, 37, 63–66, doi:10.1130/G25318A.1.
- Toomey, D. R., and G. R. Foulger (1989), Tomographic inversion of local earthquakes data from the Hengill-Greindalur Central Volcano Complex, Iceland, *J. Geophys. Res.*, 94, 17,497–17,510, doi:10.1029/JB094iB12p17497.
- Um, J., and C. H. Thurber (1987), A fast algorithm for two-point seismic ray tracing, *Bull. Seismol. Soc. Am.*, 77, 972–986.
- Waldhauser, F., and D. P. Schaff (2008), Large-scale relocation of two decades of northern California seismicity using cross-correlation and double-difference methods, *J. Geophys. Res.*, 113, B08311, doi:10.1029/2007JB005479.
- Weiland, C. M., L. K. Steck, P. B. Dawson, and V. A. Korneev (1995), Nonlinear teleseismic tomography at Long Valley Caldera, using three-dimensional minimum travel time ray tracing, *J. Geophys. Res.*, 100(B10), 20,379–20,390, doi:10.1029/95JB01147.
- Wessel, P., and W. H. F. Smith (1991), Free software helps map and display data, *Eos Trans. AGU*, 72, 441, doi:10.1029/90EO00319.

I. Bianchi, Department of Meteorology and Geophysics, University of Vienna, Althanstraße 14, A-1090, Vienna, Austria.

C. Chiarabba, P. De Gori, and D. Seccia, INGV, CNT, Via di Vigna Murata, 605, I-00143, Rome, Italy. (danilo.seccia@ingv.it)

D. P. Hill, U.S. Geological Survey, 345 Middlefield Rd., Menlo Park, CA 94025, USA.